


















<b>Publication Year</b>	2024
<b>Acceptance in OA</b>	2025-01-30T18:29:53Z
<b>Title</b>	The TRAPUM Small Magellanic Cloud pulsar survey with MeerKAT - II. Nine new radio timing solutions and glitches from young pulsars
<b>Authors</b>	Carli, E., Antonopoulou, D., BURGAY, MARTA, Keith, M. J., Levin, L., Liu, Y., Stappers, B. W., Turner, J. D., Barr, E. D., Breton, R. P., Buchner, S., Kramer, M., Padmanabh, P. V., POSSENTI, ANDREA, Venkatraman Krishnan, V., Venter, C., Becker, W., Maitra, C., Haberl, F., Thongmearkom, T.
<b>Publisher's version (DOI)</b>	10.1093/mnras/stae1897
<b>Handle</b>	<a href="http://hdl.handle.net/20.500.12386/35752">http://hdl.handle.net/20.500.12386/35752</a>
<b>Journal</b>	MONTHLY NOTICES OF THE ROYAL ASTRONOMICAL SOCIETY
<b>Volume</b>	533

# The TRAPUM Small Magellanic Cloud pulsar survey with MeerKAT – II. Nine new radio timing solutions and glitches from young pulsars

E. Carli <sup>1,★</sup>, D. Antonopoulou,<sup>1</sup> M. Burgay <sup>2</sup>, M. J. Keith <sup>1</sup>, L. Levin,<sup>1</sup> Y. Liu <sup>1</sup>, B. W. Stappers <sup>1</sup>, J. D. Turner <sup>1</sup>, E. D. Barr <sup>3</sup>, R. P. Breton <sup>1</sup>, S. Buchner,<sup>4</sup> M. Kramer <sup>3</sup>, P. V. Padmanabh <sup>3,5,6</sup>, A. Possenti,<sup>2</sup> V. Venkatraman Krishnan <sup>3</sup>, C. Venter <sup>7</sup>, W. Becker,<sup>3,8</sup> C. Maitra <sup>8</sup>, F. Haberl <sup>8</sup> and T. Thongmeearkom <sup>1,9</sup>

<sup>1</sup>*Jodrell Bank Centre for Astrophysics, Department of Physics and Astronomy, The University of Manchester, Manchester M13 9PL, UK*

<sup>2</sup>*INAF-Osservatorio Astronomico di Cagliari, via della Scienza 5, I-09047 Selargius, Italy*

<sup>3</sup>*Max-Planck-Institut für Radioastronomie, Auf dem Hügel 69, D-53121 Bonn, Germany*

<sup>4</sup>*South African Radio Astronomy Observatory (SARAO), 2 Fir Street, Black River Park, Observatory, Cape Town 7925, South Africa*

<sup>5</sup>*Max-Planck-Institut für Gravitationsphysik (Albert-Einstein-Institut), D-30167 Hannover, Germany*

<sup>6</sup>*Leibniz Universität Hannover, D-30167 Hannover, Germany*

<sup>7</sup>*Centre for Space Research, Private bag X6001, North-West University, Potchefstroom 2520, South Africa*

<sup>8</sup>*Max-Planck-Institut für extraterrestrische Physik, Gießenbachstraße 1, D-85748 Garching bei München, Germany*

<sup>9</sup>*National Astronomical Research Institute of Thailand, Don Kaeo, Mae Rim, Chiang Mai 50180, Thailand*

Accepted 2024 July 30. in original form 2024 June 26

## ABSTRACT

We report new radio timing solutions from a 3-yr observing campaign conducted with the MeerKAT and Murriyang telescopes for nine Small Magellanic Cloud pulsars, increasing the number of characterized rotation-powered extragalactic pulsars by 40 per cent. We can infer from our determined parameters that the pulsars are seemingly all isolated, that six are ordinary pulsars, and that three of the recent MeerKAT discoveries have a young characteristic age of under 100 kyr and have undergone a spin-up glitch. Two of the sources, PSRs J0040–7337 and J0048–7317, are energetic young pulsars with spin-down luminosities of the order of  $10^{36}$  erg s<sup>−1</sup>. They both experienced a large glitch, with a change in frequency of about 30 μHz, and a frequency derivative change of order  $-10^{-14}$  Hz s<sup>−1</sup>. These glitches, the inferred glitch rate, and the properties of these pulsars (including potentially high inter-glitch braking indices) suggest these neutron stars might be Vela-like repeating glitchers and should be closely monitored in the future. The position and energetics of PSR J0048–7317 confirm it is powering a new pulsar wind nebula (PWN) detected as a radio continuum source; and similarly the association of PSR J0040–7337 with the PWN of supernova remnant (SNR) DEM S5 (for which we present a new *Chandra* image) is strengthened. Finally, PSR J0040–7335 is also contained within the same SNR but is a chance superposition. It has also been seen to glitch with a change of frequency of  $10^{-2}$  μHz. This work more than doubles the characterized population of SMC radio pulsars.

**Key words:** stars: neutron – pulsars: general – pulsars: individual: PSR J0040–7326, PSR J0040–7335, PSR J0040–7337, PSR J0043–7319, PSR J0044–7314, PSR J0048–7317, PSR J0051–7204, PSR J0054–7228, PSR J0105–7208 – ISM: supernova remnants – galaxies: individual: Small Magellanic Cloud – Magellanic Clouds.

## 1 INTRODUCTION

The Small and Large Magellanic Clouds (SMC and LMC) are the only galaxies outside our own in which radio pulsars have been discovered to date. They are nearby galaxies that are unobstructed by the Milky Way’s (MW) Galactic plane. Indeed, the SMC is just 60 kpc away (Karachentsev et al. 2004), and the expected MW dispersion measure (DM) contribution in its direction is low: about 30 pc cm<sup>−3</sup> according to the YMW2016 electron density model (Yao, Manchester & Wang 2017), and 42 pc cm<sup>−3</sup> according to the NE2001

model (Cordes & Lazio 2004). Of the nearly 3400 radio pulsars that have been discovered, only 38 are extragalactic.

14 are in the SMC, discovered by McConnell et al. (1991) (one pulsar), Crawford et al. (2001) (one), Manchester et al. (2006) (three), Titus et al. (2019) (two), and Carli et al. (2024) (seven). Their median DM is approximately 110 pc cm<sup>−3</sup>.

TRAPUM (TRANSients and Pulsars with MeerKAT) is a Large Survey Project of the MeerKAT telescope ([trapum.org](http://trapum.org), Stappers & Kramer 2016). The collaboration has already discovered over 200 pulsars<sup>1</sup> in the MW (e.g. Ridolfi et al. 2022; Clark et al. 2023;

\* E-mail: [emma.carli@outlook.com](mailto:emma.carli@outlook.com)

<sup>1</sup><http://trapum.org/discoveries/>

Padmanabh et al. 2023). In Carli et al. (2024) (Paper I of this series), TRAPUM reported the discovery of seven new radio pulsars in the SMC. One of TRAPUM’s science goals is to characterize these extragalactic pulsars to better understand their population. The SMC has undergone recent episodes of star formation (Harris & Zaritsky 2004), which should allow the detection of a higher proportion of short-lived and young objects than in the MW’s older population, such as pulsar wind nebulae (PWNe), and a high density of supernova remnants (SNRs) as shown in e.g. Cotton et al. (2024) and Maggi et al. (2019).

Indeed, we presented the discovery of the first two radio pulsars in the SMC to be associated with PWNe in Paper I: PSR J0040–7337 in the SNR DEM S5 (Haberl et al. 2000; Payne et al. 2007; Alsaberi et al. 2019) and PSR J0048–7317 in a new PWN (Cotton et al. 2024). The associations were based on preliminary positions and, in the case of PSR J0048–7317, an age estimate from two survey observations.

In addition, two young pulsars (not accretion-powered) have been discovered, via their X-ray pulsations only, in the SMC: the magnetar CXOU J010043.1–721134 by Lamb et al. 2002 (recently associated with a new SNR by Cotton et al. 2024) and the rotation-powered pulsar J0058–7218 by Maitra et al. (2021) (see also Carli et al. 2022). The latter is embedded in a PWN in the SNR IKT 16 (Inoue, Koyama & Tanaka 1983; Mathewson et al. 1984; Owen et al. 2011; Maitra et al. 2015). There are no other rotation-powered pulsars known in the other 19 SNRs of the SMC.

Pulsar timing is the process of measuring the evolution of a pulsar’s rotation rate over a period of time. It enables the position and spin period derivatives of the neutron star to be measured precisely, and, assuming a magnetic dipole model (Gold 1968), allows a simplified characterization of its age, magnetic field, and rotational energy loss rate (see Lorimer & Kramer 2005).

It also monitors variations in the pulsars’ properties, due for example to the effects of binary motion. The SMC hosts the only known extragalactic binary pulsar:<sup>2</sup> PSR J0045–7319, an ordinary pulsar with a massive main-sequence B star companion. It was discovered by McConnell et al. (1991) and its binarity was revealed after several years of timing by Kaspi et al. (1994).

Further, this monitoring of the spin period of pulsars enables the detection of glitches. Most glitches are detected in young, energetic pulsars (e.g. Basu et al. 2022) and consist of a sudden spin-up event. They might be caused by the unpinning of superfluid vortices in the neutron star interior, although this is still debated (Anderson & Itoh 1975, see Antonopoulou, Haskell & Espinoza 2022 for a review). Characterizing and reporting these events is important for studies of superdense matter states (e.g. Lyne, Shemar & Graham Smith 2000; Ho et al. 2015; Antonopoulou et al. 2022). There are only two extragalactic pulsars that have been observed to glitch, both in the LMC. These are PSR J0537–6910, only detected in X-ray pulsations in a PWN in the SNR N157B (Wang & Gotthelf 1998; Wang et al. 2001); and the ‘Crab pulsar twin’ PSR J0540–6919 in the PWN with SNR 0540–69.3 (Manchester, Staveley-Smith & Kesteven 1993b; Gotthelf & Wang 2000; Brantseg et al. 2013), the only known extragalactic multiwavelength pulsar (Seward, Harnden & Helfand 1984; Middleditch & Pennypacker 1985; Manchester et al. 1993a; Marshall et al. 2016). Recently, a possible ‘antiglitch’ – a sudden spin-down event – has been witnessed in PSR J0540–6919, the first for a rotation-powered pulsar (Tuo et al. 2024). PSR J0537–6910 is not only the fastest-spinning young pulsar known, but also the most

prolific glitching pulsar known, with frequent, large spin-ups and a unique, strong correlation between the glitch size and the time until the following event (Middleditch et al. 2006; Antonopoulou et al. 2018; Ferdman et al. 2018). Overall, the exotic behaviour revealed by extragalactic pulsar timing emphasizes the importance of monitoring young extragalactic systems.

In this paper, we detail the results of a 3-yr radio timing campaign to characterize the pulsar discoveries from the Carli et al. (2024) (Paper I) and Titus et al. (2019) surveys of the SMC as part of TRAPUM’s goal to expand the known sample of the extragalactic neutron star population. We describe our observations with the MeerKAT and Murriyang telescopes in Section 2. The timing methods and solutions of non-glitching pulsars are reported in Sections 3 and 4, respectively. All the pulsar discoveries of Paper I which we now determine to be young<sup>3</sup> have glitched during our monitoring. We describe our modelling of these events and their implications in Section 5. The parameters derived from the radio timing solutions enable us to interpret the pulsars’ associations which we discuss in Section 6.

## 2 OBSERVATIONS

We collated a data set of observations for nine SMC radio pulsars with no timing solutions: seven pulsar discoveries from Carli et al. (2024) (PSRs J0040–7326, J0040–7335, J0040–7337, J0044–7314, J0048–7317, J0054–7228, and J0105–7208) and two from Titus et al. (2019) (PSRs J0043–7319 and J0051–7204 which were localized in Paper I). The observations span nearly 3 yr in total. We recorded data with the MeerKAT 64-antenna radio interferometer in South Africa, described in Section 2.1, and the 64-m single dish Murriyang telescope at Parkes, Australia (Section 2.2). We included the survey data of all the new pulsars from Paper I, including the discovery data. The details of these observations are reported there. We did not use the single Murriyang discovery observation for PSR J0043–7319 and PSR J0051–7204 of Titus et al. (2019) to keep the timing data sets to a single observatory.

### 2.1 MeerKAT observations

We conducted three pseudo-logarithmically spaced timing campaigns with the full array of the MeerKAT telescope at *L* band (central frequency of 1284 MHz, Lehmsiek & Theron 2012). The data were recorded on the APSUSE on-site computing cluster (Accelerated Pulsar Searching User-Supplied Equipment, used by TRAPUM, Barr 2017; Padmanabh 2021) with a bandwidth of 856 MHz split into 4096 channels and a sampling time of 76  $\mu$ s, in SIGPROC filterbank format (Lorimer 2008) with no coherent de-dispersion. The observations started with a short separation (half a day to a day) between observations to ensure phase connection. The separation between observations then increased in a pseudo-logarithmic fashion to an intended total time span of about 9 months per campaign.

We used the Filterbanking Beamformer User Supplied Equipment (FBFUSE, used by TRAPUM, Barr 2017; Chen et al. 2021; Padmanabh 2021) to form several simultaneous MeerKAT closely packed coherent beams on and around the location of each timed pulsar within a pointing. We initially employed the SEEKAT multibeam localization software (Bezuidenhout et al. 2023) to obtain a more precise position than had been possible from the discovery data. Then, we repeated the process by centring the next observation’s

<sup>2</sup>There are no known extragalactic compact binaries with variations on shorter time-scales (or millisecond pulsars, which are often found in such systems).

<sup>3</sup>With a characteristic age under 100 ky.

beam tiling on the new localization. This increased the S/N of the pulsars (reducing the integration time from 30 to 10–15 min) and provided a precise pre-timing position. When this precision was sufficient, pulsars were observed with a single beam. The accurate position obtained is crucial in reducing the timing baseline where a covariance between the spin period derivative and position error is present to about 6 to 9 months. Typically, with larger position errors, this covariance would not be eliminated for closer to a year.

The first campaign aimed to determine a timing solution for the first six Carli et al. (2024) discoveries and the two Titus et al. (2019) discoveries. A pseudo-logarithmic cadence was adopted from the third observation. The campaign started in 2022 February and ended in 2022 December with a total of 11 *L*-band observations of each of two pointing positions. Pointing ‘SMCTIMING1a’<sup>4</sup> comprised the pulsars J0040–7326, J0040–7335, J0040–7337, J0044–7314, J0048–7317, J0043–7319, and the bright known pulsar J0045–7319 (McConnell et al. 1991) for testing purposes. We used the multibeam capability of the TRAPUM backends to time these pulsars simultaneously. Pointing ‘SMCTIMING1b’ recorded pulsars J0054–7228 and J0051–7204.

As part of this campaign, a single 40-min observation of ‘SMCTIMING1a’ and ‘SMCTIMING1b’ was completed with MeerKAT’s Ultra High Frequency receiver (UHF, 544–1088 MHz, Lehmen-siek & Theron 2014) with a bandwidth of 544 MHz split into 4096 channels and a sampling time of 60  $\mu$ s to characterize eight pulsars in this band. The resulting pulse profiles are shown in Section 4.2. The data were not used as part of the timing solution.

The second pseudo-logarithmically spaced MeerKAT campaign consisted of observations to obtain the timing solution for a later discovery, PSR J0105–7208. It is spatially separated from the other pulsars in this work, and thus was timed on its own, at the centre of the ‘SMCTIMING2a’ pointing location. The campaign started in 2022 December and ended in 2023 January with a total of eight observations. One observation was affected by lightning but could still be used. The rest of the campaign was observed with Murriyang, which is described in the next section.

The third pseudo-logarithmically spaced MeerKAT campaign was performed to provide a phase-connected post-glitch timing solution for PSR J0040–7335 and PSR J0040–7337 as they proved difficult to time with Murriyang (described in the next section). The campaign started in 2023 June and ended in 2023 August with a total of seven observations of one pointing position. Pointing ‘SMCGLITCHERS’ was aimed directly at PSR J0040–7335 to obtain maximal gain on this faint pulsar. Taking advantage of the multibeam capacity of TRAPUM, we also timed all the nearby pulsars that were in the field of ‘SMCPOINTING1a’.

## 2.2 Murriyang observations

We reported in Paper I that, upon discovery of a pulsar, we attempted to obtain detections in archival Murriyang data. None of the pulsars could be detected. This prevented the extension of our timing solutions into the pre-discovery past. We also conducted our own observations with Murriyang, using the Ultra-Wide-band Low receiver (UWL, Hobbs et al. 2020), covering a frequency range from 0.7 to 4 GHz. Most pulsar discoveries of Paper I are too faint to be detected in 1 h or less at Murriyang with the UWL.

We began observing our brightest discovery, PSR J0048–7317, with Murriyang early in the MeerKAT SMC survey. This was initially done using Director’s Time, then registered under Project P1054 (Follow-up of pulsar discoveries from MeerKAT searches) from 2021 June. PSR J0048–7317 then became part of the P1054 project from 2021 September until today. Initially, these (usually) 1-h long observations were performed with a close cadence to obtain a first timing solution, which revealed that the pulsar was young, then monthly to monitor the pulsar for possible glitches and timing noise. Extra observations were performed using Director’s Time between 2022 September and 2023 March under project code PX092<sup>5</sup> to obtain a new coherent timing solution after the pulsar underwent a large glitch in 2022 May. Search mode (64  $\mu$ s sampling, 3328 frequency channels, no polarization) was initially used while there was no timing solution, then followed by search and fold mode from 2021 December to 2022 May, and in fold mode with coherent de-dispersion (1024 pulse profile bins, 30 s sub-integrations, 3328 frequency channels, all Stokes parameters recorded) only afterwards when it was deemed reliable. This amounted to a total of 37 successful observations with only one non-detection.

After the first MeerKAT timing campaign determined that PSR J0040–7335 and PSR J0040–7337 were young pulsars, we began monitoring them with Murriyang Director’s Time to reveal possible glitches or timing noise. They were observed in the same beam, under the target names ‘PWN0040-7337’ or ‘J0040-7335’, in search mode (128  $\mu$ s sampling, 3328 frequency channels) to be able to fold both pulsars from the same observation. The observations began in 2022 January under P1054, then were attributed the Director’s Time project code PX096 from 2022 December. The flux of the pulsars was very variable, and often too faint to be detected in short observation times. From 2023 March to May a denser campaign was attempted to obtain a coherent timing solution after both pulsars glitched (PSR J0040–7335 glitched in 2022 December, PSR J0040–7337 glitched in 2023 February). This was taken over at MeerKAT due to insufficient sensitivity. In total, 14 observations were performed successfully until 2023 December, with integration times between 20 min and 4 h.

Finally, after a successful test in 2022 November, two 1.5 h PX096 search mode observations were conducted in 2023 March and May to extend the MeerKAT pseudo-logarithmically spaced campaign on PSR J0105–7208. They yielded weak detections, particularly affected by radio frequency interference (RFI). In 2023 August, a test 1.5 h fold mode observation was unsuccessful in detecting the pulsar, again due to RFI.

The only pulsar discoveries of Paper I that were not observed with Murriyang are J0040–7326 and J0044–7314. The two Titus et al. (2019) discoveries PSR J0051–7204 and PSR J0043–7319 were also only observed with MeerKAT. These four pulsars were timed as part of the multibeam targets described in the previous section. A test Murriyang observation of PSR J0054–7228 was performed on 2021 June 7 but the pulsar was deemed too weak to observe regularly there.

## 3 DATA REDUCTION

In this section, we describe the methods employed to reduce the data of all nine pulsars in this study. We also describe the fitting analysis performed to determine the spin and astrometric parameters of the

<sup>4</sup>These target names can be used to search the records of the [SARAO web archive](#).

<sup>5</sup>Except for the initial 2022 September Director’s Time observation that was recorded under P1054.

six pulsars in this study that have not glitched, resulting in phase coherent radio timing models.

### 3.1 MeerKAT data reduction and timing solution fitting

For each MeerKAT observation, the RFI in the raw data were cleaned using PULSARX's `filter` (Men et al. 2023). We then created a high-resolution phase-folded archive with DSPSR (Van Straten & Bailes 2011), downsampling the raw data to 512 channels, 10-s sub-integrations, and 1024 phase bins. The initial phase folding parameters were the discovery localization,<sup>6</sup> DM, and period of each pulsar (which are stated in Paper I). The folded data were further RFI-cleaned with CLFD (Morello 2023), and if required, additional manual cleaning was performed using PSRCHIVE (Hotan, van Straten & Manchester 2004). Initially, before an ephemeris was obtained, we searched for the highest S/N total profile of each observation with PSRCHIVE's `pdmp` tool if deemed necessary. We optimized the sum of the phase-folded data over a small range of periods and DMs. Each observation's data were independently re-folded with these parameters if needed. Eventually, ephemerides were used to re-fold all the high-resolution archives with a single ephemeris. We thus obtained a single (frequency and time summed) pulse profile for each observation with PSRCHIVE's `pam` tool.

A noiseless template profile was first fitted to the discovery pulse profile of each pulsar, and later a new template was made from a higher S/N detection. This was done using PSRCHIVE's `paas` tool, manually adding von Mises function components (see Section 4.2). The final template profile was built from adding up all<sup>7</sup> *L*-band observations in phase using the ephemerides stated in Section 4 with PSRCHIVE's `psradd` tool, and optimizing the archive over  $20 \text{ pc cm}^{-3}$  with `pdmp` to determine the final DM value of each pulsar exclusively timed at MeerKAT.

We then fitted a topocentric Time of Arrival (ToA) and ToA error to each phase-added observation with PSRCHIVE's `pat` tool. We used the Fourier domain algorithm with Markov chain Monte Carlo to cross-correlate the noiseless template to each observation's pulse profile. For the non-glitching pulsars, we fitted a timing model containing celestial coordinates and pulsar spin parameters to the ToAs with TEMPO2 (Edwards, Hobbs & Manchester 2006; Hobbs, Edwards & Manchester 2006). TEMPO2 transformed our topocentric ToAs to the Solar system barycentre using the Jet Propulsion Laboratory's DE405 Solar system ephemeris (Standish 1998). We used the TEMPO2 model version number 5.00 and the TT(TAI) clock correction procedure. The model parameters and residuals are presented in Section 4.1.

The pulse width of the pulsars was obtained from the final summed pulse profile of all observations (that was used to determine ToAs). The initial `paas` model components were refined and debased using PSRSALSA's `fitvonMises` tool (Weltevrede 2016). Then, we added noise to the refined model profile using the off-pulse noise statistics of the summed profile. We again refined the model, fitting a pulse width at 50 per cent of the peak intensity to the model with added noise, and repeated this process 1000 times. The mean and standard deviation of the resulting width distribution are quoted in Section 4.2.

### 3.2 Murriyang data reduction

The reduction of the Murriyang observations was performed similarly to the steps detailed in the previous section. The differences

in processing are detailed here. `filter` was not applied to the observations of PSR J0048–7317 and DSPSR's `digifil` was used to merge raw data time segments (search mode), unless the data were already folded online (fold mode). A static UWL channel mask was generally employed. The fold-mode data were flux calibrated using PSRCHIVE's `pac` command and flux calibrators provided by the Murriyang observatory.<sup>8</sup> Where polarization products were recorded, the fold-mode data were polarization calibrated using short noise diode recordings performed before each observation. The high-resolution stored archives have 416 channels. Due to an oversight, polarization calibration was performed on archives with this frequency resolution. When adding observations with `psradd`, the phase alignment option was used if the observations were folded with an ephemeris that contained red noise terms. The Murriyang pulse template was rotated to have its peak at the same phase as MeerKAT's, except PSR J0105–7208 for which our observations did not accumulate enough total S/N to produce a UWL pulse profile template. The DM obtained from optimizing the Murriyang phase-added observations was used as the final value for pulsars timed with both MeerKAT and Murriyang, as the wide frequency range of the UWL allowed a more precise determination<sup>9</sup> of this value than MeerKAT's *L* band, though they were consistent. Finally, we fitted a temporal jump between the two observatories with TEMPO2.

## 4 RESULTS

We obtained phase-coherent timing solutions for all nine pulsars. We present a new period–period derivative diagram for extragalactic pulsars in Fig. 1, adding all nine pulsars in this work. Their pulse profiles are discussed in Section 4.2. In Section 4.1, the timing models obtained through the methods described in Section 3 from the observations detailed in Section 2 are used to characterize the six pulsars in this study that have not glitched. The solutions for the pulsars that have glitched are given in Section 5.

### 4.1 Timing solutions: normal pulsars

The timing parameters from our best-fitting solutions for the pulsars that have not undergone a glitch are given in Table 1. The time span of the PSR J0105–7208 data is too short to fit a position, therefore we used our best SEEKAT timing observation localization (for which  $3\sigma$  errors are quoted but not used in the fit). We find that the apparent change in rotation period that would be caused by the SEEKAT position error (if the period was compared at the near and far side of the Earth's orbit) is negligible compared to the error on the first derivative of frequency for this pulsar. The DM errors quoted are obtained from a `pdmp` optimization over  $20 \text{ pc cm}^{-3}$  of the total added *L*-band observations, and are not used in fitting. We note that none of the pulsars required additional parameters from e.g. binary motion. Additional derived parameters calculated by TEMPO2: the characteristic age, surface magnetic field strength, and rotational energy loss are also given. The residuals from these best-fitting models are given in Fig. 2. The glitching pulsars' timing solutions are given in Section 5.2.

We note that two of the pulsars timed only at MeerKAT have an 'adolescent' age of around 200 kyr. The first of these, PSR J0051–7204, shows no notable timing noise. However, we

<sup>6</sup>As the MeerKAT timing observations progressed, the localizations were refined with SEEKAT as detailed in Section 2.1.

<sup>7</sup>One or two were omitted for some pulsars.

<sup>8</sup>[https://www.parkes.atnf.csiro.au/observing/Calibration\\_and\\_Data\\_Processing\\_Files.html](https://www.parkes.atnf.csiro.au/observing/Calibration_and_Data_Processing_Files.html)

<sup>9</sup>This was not done for PSR J0040–7335 and PSR J0105–7208 due to their low S/N in Murriyang observations.

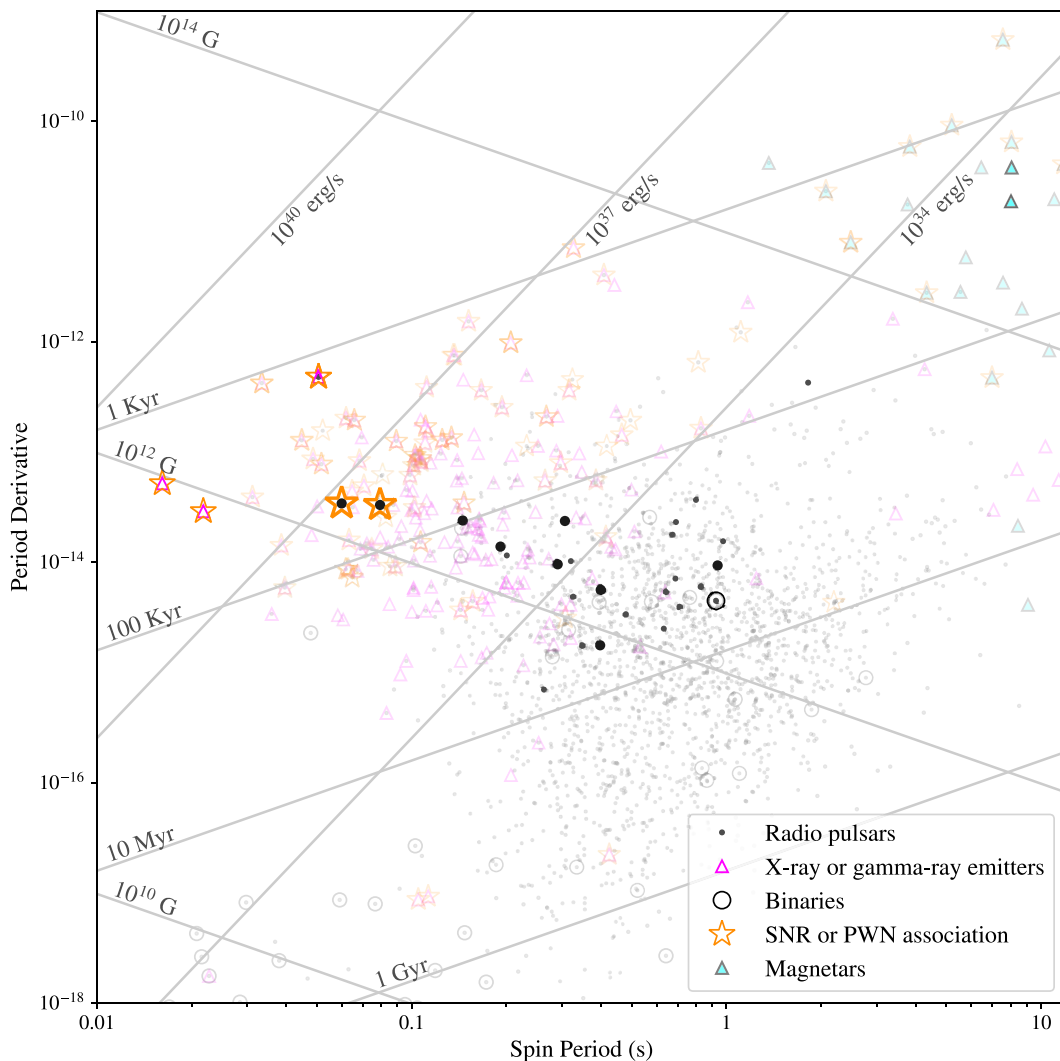


**Figure 1.** The period–period derivative diagram of non-accretion-powered pulsars is shown, with the nine pulsars characterized in this work shown as large circular markers. Previously known extragalactic pulsars are shown with smaller circular markers and the MW pulsars are shown using transparent markers. The millisecond pulsar parameter space is not shown as there are no such known extragalactic pulsars. Galactic rapidly rotating radio transients and Galactic pulsars in globular clusters are also not plotted for the same reason. The data were retrieved from the ATNF Pulsar Catalogue version 2.2.0 (Manchester et al. 2005). Lines of constant characteristic age, spin-down luminosity, and surface magnetic field are shown. The population of pulsars in the SMC will be studied in Paper III. This figure was produced with the PRESTO package.

could not phase-connect the discovery observation of the second adolescent pulsar PSR J0105–7208, which occurred 5 months before the beginning of the radio timing campaign presented here. We would normally expect the timing solution to successfully extrapolate back to the discovery observation, as the phase-connected time span is of similar length as the extrapolation period, thus we cannot exclude a glitch or timing noise in that observation gap. Furthermore, PSR J0043–7319, which has a characteristic age of 1.6 Myr, requires a  $\ddot{\nu}$  component to fit the residuals, which is about two orders of magnitude larger than the expected contribution from dipole braking for a braking index of 3. The origin of this is not known, but a glitch or timing noise are again not excluded.

#### 4.2 Pulse profiles

We present the total summed pulse profiles of the pulsars in Fig. 3. We noted no significant pulse profile shape change between the

MeerKAT *L* band/UHF and Murriyang UWL band during observations, except for a longer scattering tail for PSR J0040–7335 in the UHF band.

We also present the polarization profile of PSR J0048–7317 over the UWL band in Fig. 4. We first performed the steps described in Section 3.2 to obtain a total flux and polarization-calibrated phase-folded data archive with 1024 pulse profile bins and 416 frequency channels from 26 fold-mode Murriyang observations. We performed a search for rotation measure (RM) using PSRSALSA’s `rmsynth` (Weltevrede 2016) over  $\pm 6 \times 10^4 \text{ rad m}^{-2}$  [in case of a large PWN contribution, see e.g. Piro & Gaensler 2018 and the high-RM fast radio bursts with persistent radio sources like FRB 20121102A (Michilli et al. 2018)]. At the minimum, central, and highest frequencies of the UWL band, an RM of  $\pm 381$ ,  $\pm 1.5 \times 10^4$ , and  $\pm 7.5 \times 10^4 \text{ rad m}^{-2}$  is required to cause a rotation of  $\frac{\pi}{2}$  rad in a frequency channel, respectively.



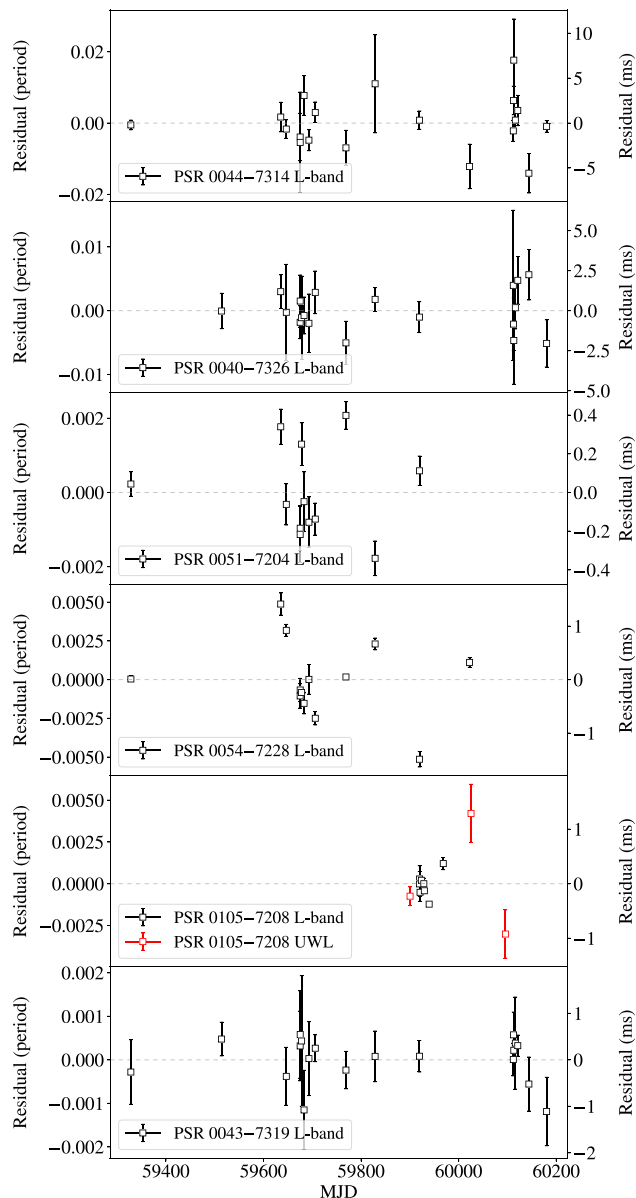


**Figure 2.** The residuals of the TEMPO2 timing model for all six non-glitched pulsars in this study. UHF ToAs, very weak detections, and observations compromised by RFI were not included.

The known range of RMs in the SMC spans  $-57$  to  $+128$   $\text{rad m}^{-2}$  (Johnston et al. 2021), and this can result in 0.7–3.6 rotations across the UWL band.

We were not able to constrain the RM, possibly due to the polarized S/N being too low and/or the frequency resolution too coarse. The RM can reduce the linear polarization fraction, thus we can only provide a lower limit on the linear polarization fraction of the total pulse profile of 6 per cent, which we estimated using PSRCHIVE’s `psrstat`. The circular polarization fraction is about 20 per cent. Cotton et al. (2024) weakly detected a circular polarization fraction of 11 per cent at the  $2\text{--}3\sigma$  level in their image of the head of the nebula. If the circular polarization fraction being larger than the linear fraction was an intrinsic property of the emission, this would be the first such case among extragalactic pulsars (Johnston et al. 2021), and though frequency-dependent, it is also relatively uncommon

among non-recycled galactic pulsars (e.g. Serylak et al. 2021; Oswald et al. 2023). We have not yet accumulated enough polarized S/N to measure the polarization Position Angle (PA) variation across the pulse.

## 5 YOUNG PULSAR GLITCHES

### 5.1 Glitch and red noise parameters estimation

To model glitch and red noise parameters, we used the software `RUN_ENTERPRISE` (Ellis et al. 2020; Keith, Nițu & Liu 2022), a Bayesian timing parameter estimation toolkit, as expanded by Liu et al. (2024) to include glitch parameters. The fitting process is described in detail in Liu et al. (2024). We input initial solutions obtained as described in Section 3 with an initial glitch size fitted with TEMPO2, as a starting point for the Bayesian parameter estimation. We tested two models on PSR J0048–7317 and PSR J0040–7337: a single glitch of permanent changes in frequency  $\Delta\nu$  (Hz) and spin-down rate  $\Delta\dot{\nu}$  ( $\text{Hz s}^{-1}$ ), with or without a single exponential relaxation term (see equation 1). We did not include in our analysis a glitch-induced change in the second-order frequency derivative,  $\Delta\ddot{\nu}$ , as initial modelling showed that it was consistent with zero. Likewise, we did not include a second, longer term exponential recovery (with a time-scale of up to 1000 d). Indeed, the prior on the second decay time was either too large to be well sampled, or resulted in an unconstrained decay time and amplitudes consistent with zero for the second exponential recovery.

The glitch model is thus expressed as

$$\Delta\phi = \Delta\nu\Delta t + \frac{1}{2}\Delta\dot{\nu}\Delta t^2 + (1 - e^{-\Delta t/\tau_{\text{decay}}})\Delta\nu_{\text{decay}}\tau_{\text{decay}}, \quad (1)$$

where  $\Delta\phi$  is the difference in predicted phase after the glitch in radians,  $\Delta t$  is the time since the glitch in seconds,  $\tau_{\text{decay}}$  is the exponential relaxation time-scale in seconds, and  $\Delta\nu_{\text{decay}}$  its amplitude in Hertz.

In the case of PSR J0040–7337, we fitted the timing model parameters to a data set of one ToA per observation. There are about 30 d between the last pre-glitch and the first post-glitch observation.<sup>10</sup> As with most large glitches, we are unable to unambiguously track the rotation of the pulsar during this observational gap, as there is a degeneracy between the glitch epoch and the number of phase wraps occurring between these ToAs. Hence the glitch epoch cannot be precisely determined (see the appendix of Basu et al. 2022 for a discussion of this), and we chose to set the number of rotations between the pre-glitch and post-glitch ToAs that resulted in the least difference in phase. This choice results in the latest possible glitch epoch as the initial input for the analysis (just before the first post-glitch ToA), and the glitch epoch prior was set as uniform within 10 d of this initial value. The prior range on the exponential recovery time-scale was set to be sampled uniformly in log-time-scale between 0.1 and 100 d, and the remaining priors were set automatically by `RUN_ENTERPRISE` as described in Liu et al. (2024), section 3.4: the red noise amplitude prior was sampled uniformly in log-scale between  $-16$  and  $-8 \text{ yr}^3$ , the red noise power-law index was sampled uniformly in linear space between 0 and 10, the exponential amplitude was sampled uniformly in linear space with a range of  $\pm 0.8$  times the input glitch step change in frequency, and

<sup>10</sup>The possibility that a glitch had occurred since the previous observation was established by inspection of the first post-glitch observation, which showed a drift in the phase of the folded pulse as a function of time.

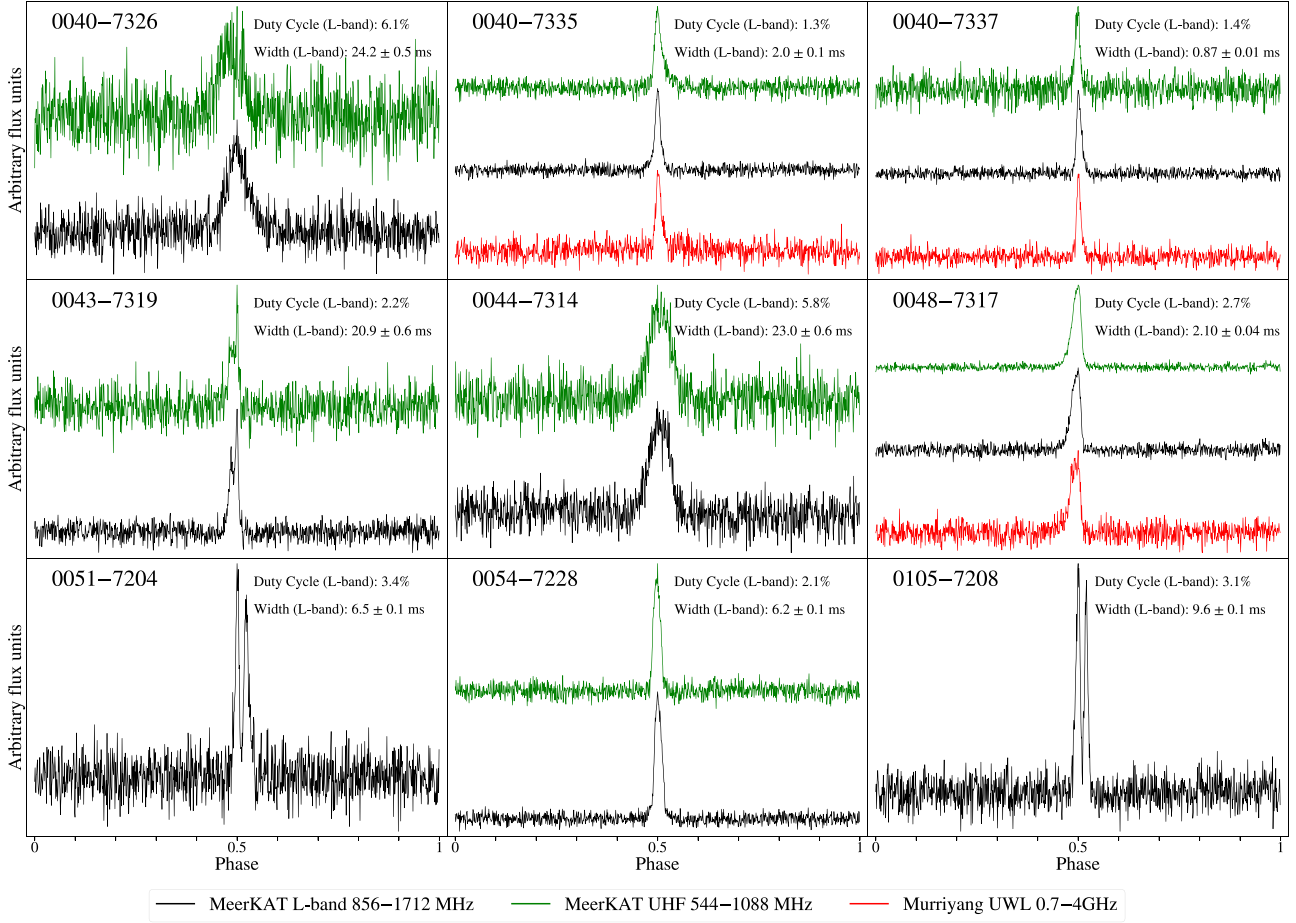


**Figure 3.** The total summed pulse profiles obtained from the observations presented in this work, except for the UWL band profile of PSR J0105–7208 which is too weak and the UHF profile for PSR J0051–7204 which was also too weak. The phase has been arbitrarily rotated to display maximum intensity at phase 0.5. The combined smearing due to sampling time and intra-channel DM smearing is negligible compared to the bin size in all bands. The duty cycle based on the width at 50 percent of the maximum intensity at *L* band is given (see Section 3.1).

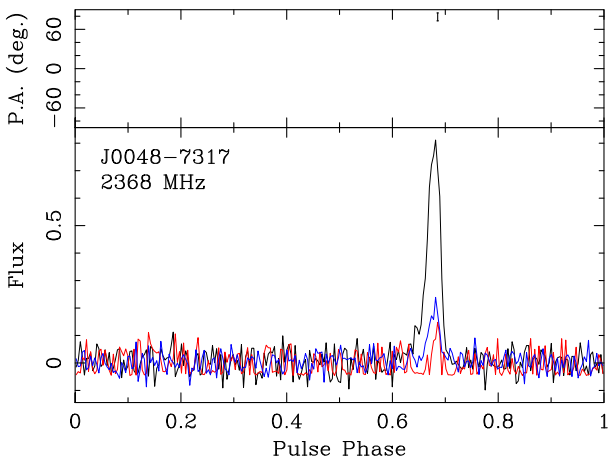


**Figure 4.** The polarization profile of PSR J0048–7317. The blue line shows circular polarization, the red line is the lower limit on linear polarization (not RM corrected), and the black line is the total intensity. We have not yet accumulated enough polarized S/N to measure the polarization PA variation across the pulse. This plot was produced with PSRCHIVE’s `psrplot`.

finally the priors in the glitch step change in frequency and frequency derivative spanned  $\pm 0.8$  times the input values, sampled uniformly in linear space.

We initially fixed the DM, temporal jump between observatories, period, and period derivatives using the values obtained as described in Section 3. The position was also fixed to the point source position (0.2–8 keV band) measured from a *Chandra* observation of the PWN,  $RA(J2000)=0^h40^m46^s.3850$ ,  $Dec.(J2000)=-73^\circ37'07''.030$  (see Section 6.1 and Fig. 11). After fitting the aforementioned glitch and red noise parameters with `RUN_ENTERPRISE`, we then input the maximum-likelihood solution into a new `RUN_ENTERPRISE` MCMC process (see Liu et al. 2024) to now simultaneously fit for position, period, period derivatives, and refine the red noise parameters, while the glitch solution remained fixed (as well as the DM and temporal jump between observatories). This produced the final ephemeris presented in Table 2.

In the case of PSR J0048–7317, the glitch occurred between observations at MeerKAT and Murriyang separated by only 3 d. The pre-glitch detection with MeerKAT had an S/N of 45.3, which we divided into 10 ToAs, and the post-glitch observation with Murriyang had an S/N of 6.5, which we divided into two ToAs. All other observations were included as single ToAs. The next observation was performed 1 month after the first post-glitch observation. Initial glitch modelling indicated that the first observation after the glitch

**Table 2.** Radio timing solution parameters for the glitched pulsars timed with MeerKAT and Murriyang. Figures in parentheses are the  $1\sigma$  uncertainties in the last digit. The derived parameters are calculated by TEMPO2. The errors in the set quantities are not used in the fit.

	Data and modelling		
Pulsar name	J0048–7317	J0040–7337	J0040–7335
MJD range	59328.1–60393.0	59585.4–60300.5	59514.1–60300.5
Data span (yr)	2.92	1.96	2.15
Number of ToAs	54	31	33
Rms timing residual ( $\mu$ s)	4554.4	14116.2	271.8
Reduced $\chi^2$ value	1.0	0.9	14.1
	Measured quantities		
Right ascension (hh:mm:ss)	00:48:56.89(9)	00:40:46.7(6)	00:40:54.59(3)
Declination (dd:mm:ss)	–73:17:46.0(4)	–73:37:07.0(25)	–73:35:53.60(8)
Pulse frequency, $\nu$ ( $s^{-1}$ )	12.608085313(5)	16.69767930(4)	6.88618772429(7)
First derivative of pulse frequency, $\dot{\nu}$ ( $10^{-12} s^{-2}$ )	–5.24925(10)	–9.4910(9)	–1.131083(20)
Second derivative of pulse frequency, $\ddot{\nu}$ ( $10^{-22} s^{-3}$ )	3.33(12)	4.9(18)	–
Glitch epoch (MJD)	59707.46(2)	60013.13(5)	–
Frequency change at glitch, $\Delta\nu$ (Hz)	$2.460(1) \times 10^{-5}$	$3.023(7) \times 10^{-5}$	$1.19(8) \times 10^{-8}$
Frequency derivative change at glitch $\Delta\dot{\nu}$ (Hz)	$-3.6(2) \times 10^{-14}$	$-7(2) \times 10^{-14}$	$-1.22(16) \times 10^{-16}$
Red noise power-law index	4.0(5)	4.3(5)	–
Red noise amplitude $yr^{\frac{3}{2}}$	–9.3(1)	–8.6(2)	–
	Set quantities		
Epoch of frequency, position, and DM determination (MJD)	59 860	59 942	59 692.1
Dispersion measure, DM ( $cm^{-3}pc$ )	292.42(7)	101.79(4)	198.27(6)
Glitch epoch (MJD)	–	–	59919.730735189097686
	Derived quantities		
Characteristic age (kyr)	38	28	97
$\log_{10}$ (Surface magnetic field strength, G)	12.21	12.16	12.27
$\log_{10}$ (Spin-down luminosity, $\dot{E}$ , $erg s^{-1}$ )	36.42	36.80	35.49
$\frac{\Delta\nu}{\nu}$	$1.95 \times 10^{-6}$	$1.81 \times 10^{-6}$	$1.7 \times 10^{-9}$
$\frac{\Delta\dot{\nu}}{\dot{\nu}}$	$7 \times 10^{-3}$	$7 \times 10^{-3}$	$1 \times 10^{-4}$

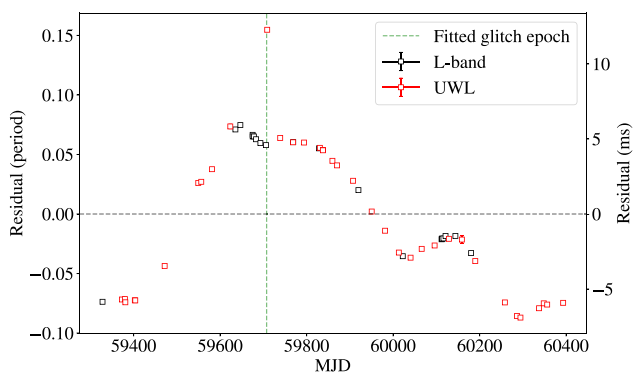


**Figure 5.** The residuals of the RUN\_ENTERPRISE timing model for PSR J0048–7317 as in Fig. 7, but with the first two observations after the glitch included. The red noise is not subtracted. A large transient residual is visible.

was not well modelled by a simple step change in frequency and frequency derivative (see Fig. 5), and hence a short-duration transient recovery was present.

We attempted to fit the transient recovery with an exponential, however since the exponential is largely determined by two residuals from a single observation, there is a wide range of valid solutions. In order to efficiently explore the parameter space, we applied a logarithm to the prior of the amplitude of the exponential, however we re-weighted the exponential amplitude posterior, multiplying it by the amplitude values. This results in a uniform space posterior distribution (revealing larger exponential recovery sizes) between

$2.5 \times 10^{-14}$  and  $2.5 \times 10^{-5}$  Hz, though the amplitudes were sampled linearly in a logarithmic prior space. The exponential time-scale prior was sampled uniformly in linear time-scale between 0.01 and 100 d. With a short-duration exponential, there may be some correlation between the glitch epoch and the exponential parameters, and hence we want to allow solutions in the full range of glitch epochs. To achieve this, we fitted for an integer number ( $\pm 10$ ) of phase wraps just prior to the first post-glitch ToA (MJD 59708.7).

We also ran a separate fit with the first two observations after the glitch removed, and the same priors and the two-stage fitting as described for PSR J0040–7337 (except that the position used was from the initial timing solution, see Section 3). To visualize long-term changes in the frequency and frequency derivative using groups of ToAs, we also used the stride fitting method (see Shaw et al. 2018) on this data set.

In the case of PSR J0040–7335, the glitch was small and phase connection appears to be preserved. As the ToAs after the glitch have quite large errors, the glitch epoch is poorly constrained. We thus set the glitch epoch to the last ToA that seemed to be consistent with the pre-glitch timing parameters and fitted only for the post-glitch change in frequency and frequency derivative with TEMPO2 (having first obtained a preliminary timing solution as described in Section 3).

## 5.2 Timing solutions: glitched pulsars

For PSR J0040–7337, an informative exponential relaxation fit cannot be performed to the sparse post-glitch data (there are about 30 d between the last pre-glitch point and the first post-glitch point, and again 20 d before the next). A model with no recovery is preferred by RUN\_ENTERPRISE, with an odds ratio of  $22 \pm 5$ .

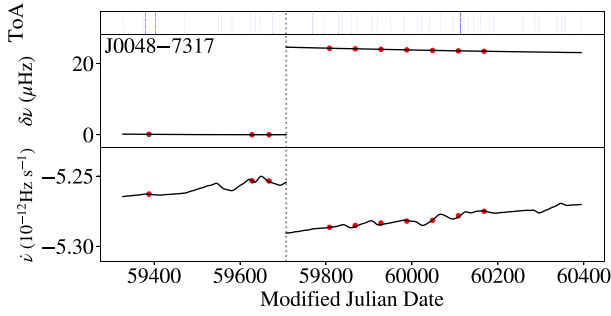


**Figure 6.** Groups (red markers) of consecutive ToAs (individually represented by blue vertical lines in the top panel) are fitted for  $\nu$  and  $\dot{\nu}$  (stride fitting method, see Section 5.1) to reveal the long-term effect of the pulsar’s spin frequency (middle panel) and spin-down rate (bottom panel) change. Our timing model (red noise included) described in Section 5.2 is represented by the black line. The error bars are smaller than the markers.

In the case of PSR J0048–7317, models containing an exponential recovery term are preferred by RUN\_ENTERPRISE when using the full data set (i.e. they have a larger likelihood); however, the constraints on the exponential time-scale and amplitude are very poor due to the low number of ToAs soon after the glitch (there is also a gap of 30 d between the first and second observation after the glitch). We show the posterior distribution of the model with exponential recovery fitted on the full data set, as described in the previous section, in Fig. 10. A strong covariance between the fitted exponential recovery time-scale and amplitude is present: the larger the amplitude, the shorter the time-scale – to vanishingly small time-scales and large amplitude. They are both poorly constrained, thus we can only provide a 95 per cent upper limit for the recovery time-scale of 22 d, and for the exponential decay amplitude the 95 per cent credible interval around the median is  $1.2^{+4.1}_{-0.4} \times 10^{-7}$  Hz. As can be seen in the first column of Fig. 10, a larger number of fitted phase wraps between the pre- and post-glitch observations results in an earlier fitted glitch epoch, with five likely glitch epoch solutions in this time range.

We therefore elected to remove the first two observations after the glitch from the data set to ignore the strongest transient effect and thus get better constraints on the permanent glitch parameters. We model the data in the same way as PSR J0040–7337 (see Section 5.1). A no-recovery model is preferred with an odds ratio of about  $2.7 \pm 0.3$ . This is the model reported in Table 2, shown in Fig. 7, and with stride fitting in Fig. 6. This model’s residuals with the first two post-glitch observations included are shown in Fig. 5.

We report the timing model parameters for the three glitching pulsars in Table 2. The DM errors quoted are obtained from a `pdmp` optimization over  $20 \text{ pc cm}^{-3}$  of the total added UWL ( $L$  band for PSR J0040–7335) observations and are not used in fitting. The RUN\_ENTERPRISE model residuals for PSR J0048–7317 and PSR J0040–7337 are shown in Figs 7 and 8, while TEMPO2’s PSR J0040–7335 model residuals are given in Fig. 9. For J0048–7317, the stride fitting results are shown in Fig. 6: the data points in the stride windows are in accordance with our model.

### 5.3 Discussion of the observed glitches

Two aspects of the aforementioned glitch activity in the SMC pulsars are worth noticing. First, the inferred glitch sizes  $\Delta\nu$  for PSRs J0048–7317 and J0040–7337 are among the largest reported, falling at the high end of the known glitch size distribution (see for example

Basu et al. 2022). Secondly, all three glitching pulsars displayed a glitch shortly after their discovery (just over a year later).

It is therefore compelling to examine how their glitch activity compares to that of the total glitching pulsar population, which predominantly consists of Galactic neutron stars.

The two SMC sources with major glitches of  $\Delta\nu \sim 10^{-5}$  Hz have relatively high spin-down rates and a similar characteristic age  $\tau_c$ , around  $10^4$  yr. On the other hand, PSR J0040–7335 has a lower  $|\dot{\nu}|$ , an age  $\tau_c \sim 10^5$  yr, and its glitch has a small inferred size. Although it is too early to draw any conclusions, the above is in general agreement with the finding that younger pulsars tend to present larger glitches (e.g. Basu et al. 2022). Glitches of small sizes like the one in PSR J0040–7335 are common in both young and old glitching pulsars (Basu et al. 2022; and we use theirs and Espinoza et al. 2011’s [Jodrell Bank Centre for Astrophysics Glitch Catalogue](#) in this analysis). Small glitches are harder to detect in the presence of timing noise and infrequent monitoring, thus their population is potentially underestimated.

Glitches are customarily regarded as rare events, with the vast majority of pulsars never seen to glitch at all. The situation changes, however, when we take into account the young characteristic age (and high  $|\dot{\nu}|$ ) of the SMC glitching sources. In the population of pulsars with  $5 \times 10^3 < \tau_c(\text{yr}) < 5 \times 10^5$ , over 30 per cent of sources have at least one reported glitch.<sup>11</sup> This demonstrates that glitches are not an uncommon feature for pulsars similar to J0040–7337, J0048–7317, and J0040–7335. Their red noise parameters are also typical (Parthasarathy et al. 2019). Moreover, of the glitching pulsars in the above age range, 52 per cent have had giant glitches, which are defined by a magnitude of  $\Delta\nu/\nu$  greater than  $10^{-6}$ ; in fact, over one-fourth of the total detected glitches are ‘giant’ according to the Jodrell Bank Glitch Catalogue.

Earlier works on glitches noted an anticorrelation between the characteristic age  $\tau_c$  of a pulsar and its glitching rate (e.g. Espinoza et al. 2011; Fuentes et al. 2017). The two most recent studies of glitch rate, which use a large sample of pulsars, confirm this relationship and explore the scaling of glitch rate with other pulsar parameters, such as  $\nu$  and  $\dot{\nu}$ , under different assumptions. The sample of the first study (Basu et al. 2022) consists of pulsars observed at the Jodrell Bank Observatory (JBO) that have at least one detected glitch. An average glitch rate is calculated for each pulsar simply as

$$r_{\text{obs}} = N_g / T_{\text{obs}}, \quad (2)$$

with  $N_g$  the total number of detected glitches and  $T_{\text{obs}}$  the total monitoring time span (which could be accurately determined for JBO observations). A negative power-law scaling with  $\tau_c$  was assumed, of the form

$$r_{\tau} \propto \tau_c^{-\alpha}, \quad (3)$$

with  $\tau_c$  in kyr; and similarly, the trend for increasing rate with increasing  $\dot{\nu}$  is described as

$$r_{\dot{\nu}} \propto |\dot{\nu}|^{\beta}, \quad (4)$$

with  $\alpha$ ,  $\beta$ , and the proportionality constants determined by the data. To somewhat compensate for the fact that glitch rates can be underestimated, only pulsars with  $r > 0.05 \text{ yr}^{-1}$  were considered (currently the smallest inferred rate is about  $0.02 \text{ yr}^{-1}$ ).

<sup>11</sup>Similarly, if we consider pulsars in the range  $5 \times 10^{-13} < |\dot{\nu}|(\text{Hz s}^{-1}) < 5 \times 10^{-11}$  (which also encompasses all three SMC glitching pulsars), about 50 per cent have known glitches.

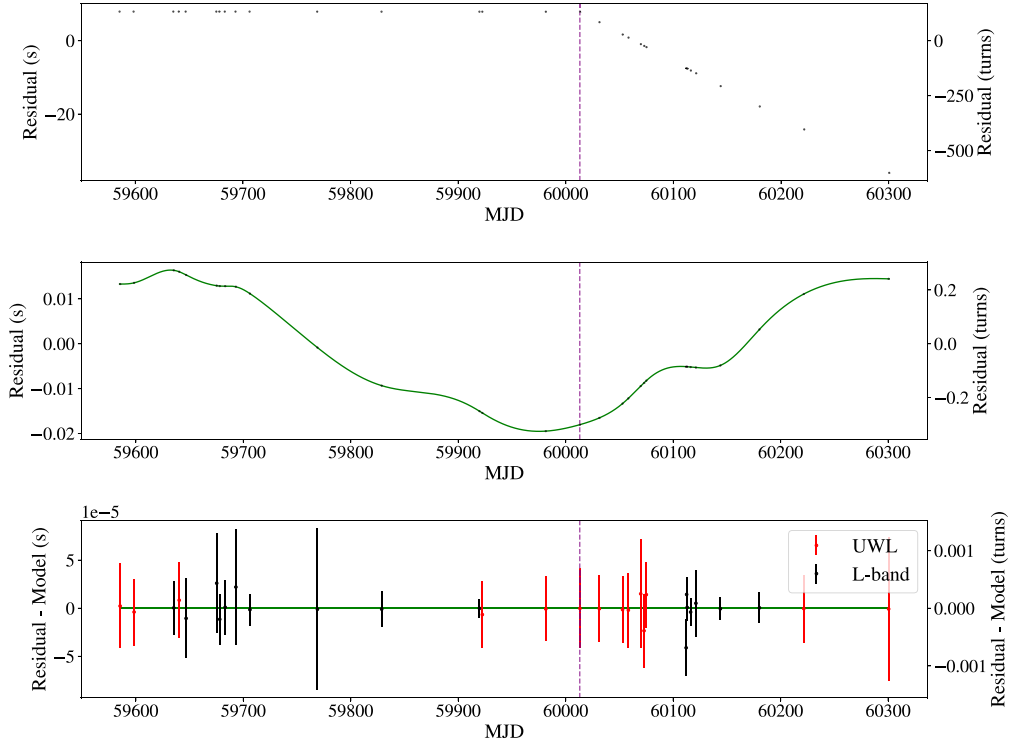


**Figure 7.** The residuals of the `RUN_ENTERPRISE` timing model for PSR J0048–7317 (see Table 2). The first two ToAs after the glitch are removed. In the first panel, the glitch parameters and red noise are not subtracted. In the second panel, the red noise is not subtracted but the glitch parameters are. In the third panel, all parameters in the model are subtracted. The fitted glitch epoch is shown as a vertical dashed line. The UHF observation was not used and two ToAs after the glitch were removed to ignore transient effects.

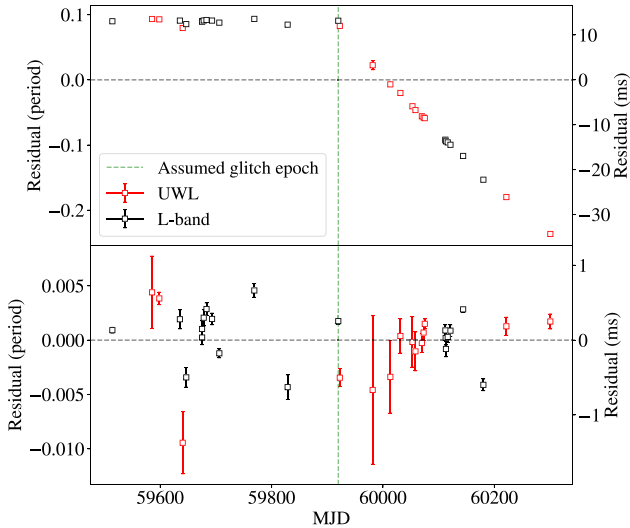


**Figure 8.** The residuals of the `RUN_ENTERPRISE` timing model for PSR J0040–7337 (see Table 2). In the first panel, the glitch parameters and red noise are not subtracted. In the second panel, the red noise is not subtracted but the glitch parameters are. In the third panel, all parameters in the model are subtracted. ToAs were obtained from 17 MeerKAT observations: 10 from the first pseudo-logarithmically spaced timing campaign (with one non-detection), and seven in the second. The UHF observation is not used. The Paper I survey data for this pulsar were accidentally deleted before it could be included here. A further 14 ToAs are obtained from Murriyang observations. The fitted glitch epoch is shown as a vertical dashed line.

The second study, Millhouse et al. (2022), assumes that glitches occur stochastically and describes glitch activity as a constant-rate Poisson process with the probability of observing  $N_g$  glitches over an observing timespan  $T_{\text{obs}}$  being

$$p(\lambda|N_g, T_{\text{obs}}) = \frac{(\lambda T_{\text{obs}})^{N_g} e^{-\lambda T_{\text{obs}}}}{N_g!} \quad (5)$$

for a pulsar with a Poisson glitch rate  $\lambda$ . This assumption is to some degree supported by observations of several frequently glitching pulsars, for which the distribution of waiting times between consecutive glitches is consistent with an exponential probability density function. Not all pulsars are consistent with this description, however. For example, the Crab pulsar observations are inconsistent with a homogeneous Poisson process (e.g. Carlin & Melatos 2019). Moreover, some neutron stars present a characteristic glitch waiting time – the Vela pulsar being a prominent example of this behaviour. Three pulsars for which the regularity in glitching patterns is well established were excluded from the study (namely, the Vela pulsar, the LMC pulsar J0537–6910, and PSR J1341–6220).

Two pulsar samples were used to calculate  $\lambda$  and infer its scaling with pulsar parameters (power-law relations with  $\nu$ ,  $\dot{\nu}$ , or a combination of the two were examined): one consisted of 174 glitching pulsars, the other additionally included 233 pulsars that have  $N_g = 0$ . The glitching pulsars sample significantly overlaps with the one used in Basu et al. (2022), but the used values of  $T_{\text{obs}}$  contained more uncertainties (see section 7 in Millhouse et al. 2022). The preferred model (based on Bayes factor) was an anticorrelation of the Poisson glitch rate  $\lambda$  with characteristic age, modelled as

$$\lambda = A(\tau_c/\tau_{\text{ref}})^{-\gamma}, \quad (6)$$

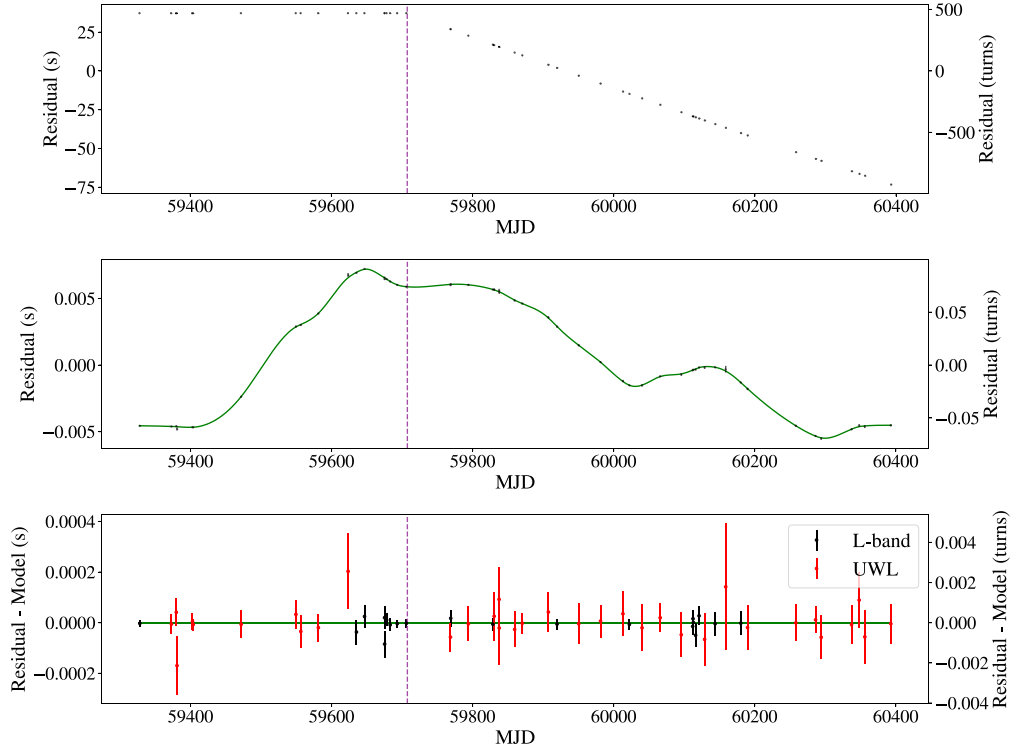


**Figure 9.** The residuals of the TEMPO2 timing model for PSR J0040–7335. The top panel shows the residuals without glitch parameters included. ToAs were obtained from 19 MeerKAT observations: one from the Paper I survey, 11 from the first pseudo-logarithmically spaced timing campaign, and seven in the second. The UHF observation is not used. A further 14 ToAs are obtained from Murriyang observations.

**Table 3.** The observed glitch rate calculated as  $r_{\text{obs}} = N_g/T_{\text{obs}}$  and the predicted glitch rate based on different assumptions (see the text for details) and using the inferred optimal parameters from Basu et al. (2022) and Millhouse et al. (2022). All rates are given in units  $\text{yr}^{-1}$ .

Pulsar name	J0048–7317	J0040–7337	J0040–7335
$r_{\text{obs}}$	0.34	0.51	0.47
$r_{\dot{\nu}}$	0.59	0.66	0.44
$r_{\tau}$	0.35	0.38	0.27
$\lambda_1$	0.14	0.15	0.11
$\lambda_0$	0.14	0.15	0.10

where  $\tau_{\text{ref}} = 1$  yr. Note that the optimal values for the parameter  $A$  in table 3 of Millhouse et al. (2022) are in units  $\text{d}^{-1}$  (Millhouse, private communication).

It is noteworthy that the power-law index ( $\alpha$  for Basu et al. 2022 and  $-\gamma$  for Millhouse et al. 2022) of the rate ( $r_{\tau}$  and  $\lambda$ , respectively) to characteristic age relationship for glitching pulsars is consistent between the two studies. Using Table 2, we calculate the observed glitch rate as in equation (2), as well as the predicted rate based on equations (3), (4), and (6). The results are presented in Table 3. The rate  $\lambda$  is denoted by index 1 when the optimal parameters for the  $N_g \geq 1$  sample are used, and by index 0 for the  $N_g \geq 0$  sample. Direct comparisons between  $r_{\text{obs}}$  and  $\lambda$  cannot be made: ideally, the median  $\lambda_{\text{obs}}$  should be calculated for each pulsar individually from a posterior distribution of  $\lambda$  based on equation (5). None the less, the predicted rates  $\lambda$  based on the Millhouse et al. (2022) relationship are of the same order of magnitude as  $r_{\text{obs}}$ , and do not lead to very low probabilities of a glitch occurring during our monitoring period.

With a single glitch per pulsar, the derived rate  $r_{\text{obs}}$  can only be a rough approximation of the true rate, under the assumption that a stationary mean rate can indeed be defined for these sources. We used the entire time interval of observations in equation (2) to calculate the  $r_{\text{obs}}$  in Table 3. Upper limits can be derived if the maximum time interval between the glitch epoch and the endpoints of the total observing span is used instead, and are close to  $1 \text{ yr}^{-1}$  for all three pulsars. Given the results in Table 3 for either the  $\dot{\nu}$  or  $\tau_c$  relationship of Basu et al. (2022), the observed rate in the SMC pulsars is in accordance with predictions based (almost exclusively) on Galactic pulsars. Therefore, while lucky, it cannot – at the moment – be considered extraordinary that a glitch was detected so soon after their discovery.

The above discussion on glitch rates does not take into account the fact that the observed glitches of PSRs J0048–7317 and J0040–7337 had amplitudes  $\Delta\nu/\nu \gtrsim 10^{-6}$ , at the higher end of the known distribution. While the analysis of Basu et al. (2022) included all JBO-observed glitching pulsars, we reiterate that the Millhouse et al. (2022) analysis excludes ‘regularly’ glitching pulsars and assumes a homogeneous Poisson process, which would lead to exponential distributions of interglitch waiting times. Typically, however, pulsars for which such a waiting time distribution is an adequate fit to observational data present at the same time a power-law-like distribution of their glitch sizes, with large events being far less common than small ones. On the other hand, large glitches are ordinary in regularly glitching pulsars. The archetype of this glitch behaviour is the Vela pulsar (PSR B0833–45, with  $\nu \simeq 11.2$ ,  $\dot{\nu} \simeq -1.567 \times 10^{-11} \text{ Hz/s}$ , and  $\tau_c \sim 10^4 \text{ yr}$ ), characterised by predominantly giant glitches ( $\Delta\nu/\nu \gtrsim 10^{-6}$ ) that occur every few years. Both PSR J0040–7337 and PSR J0048–7317 present very strong similarities to Vela, not

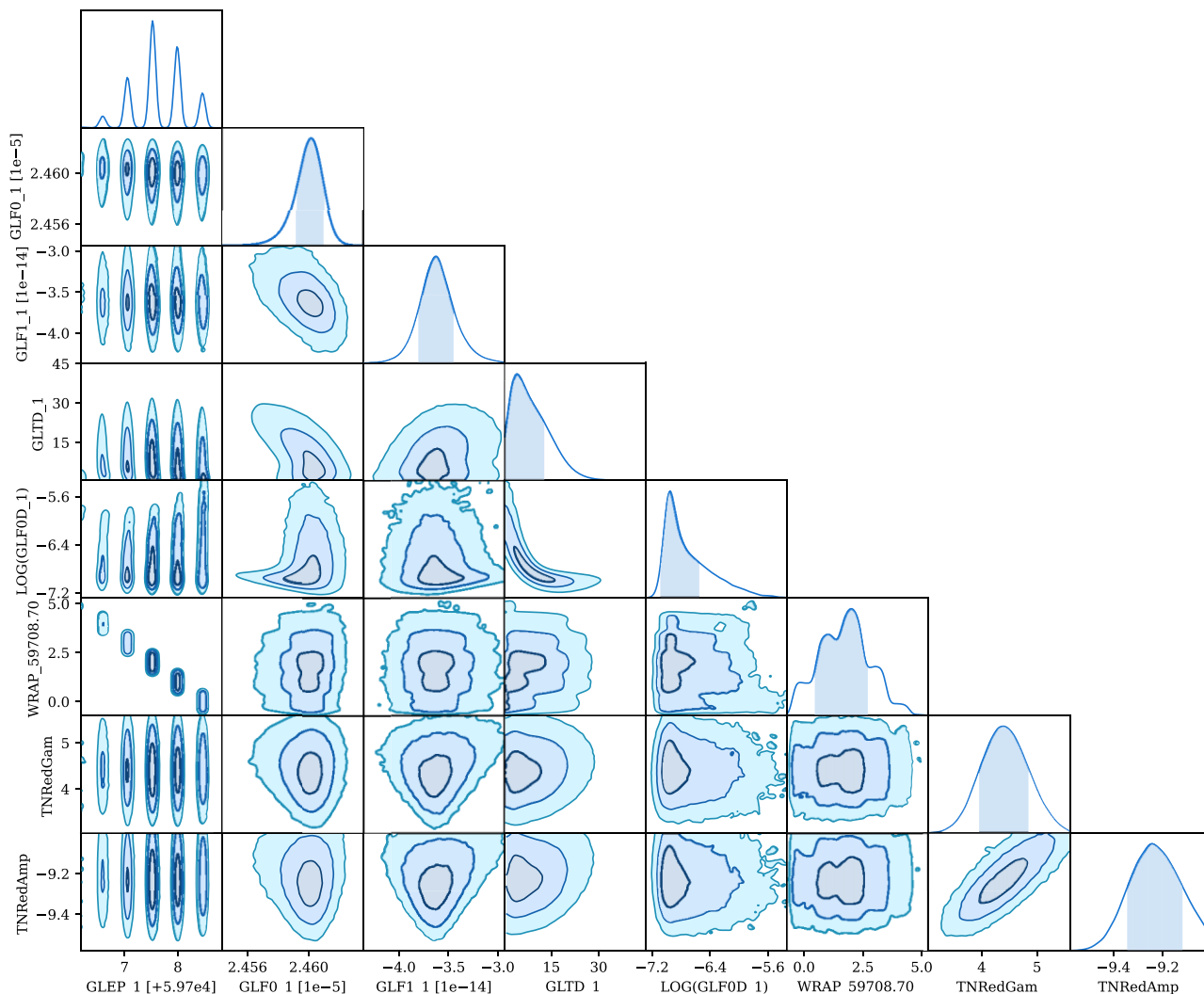


**Figure 10.** RUN\_ENTERPRISE posterior distribution of glitch models with exponential recovery, fitted to all observations of PSR J0048–7317. From left to right, the parameters on the horizontal axis are glitch epoch, permanent change in frequency ( $\Delta\nu$ ), permanent change in frequency derivative ( $\Delta\dot{\nu}$ ), exponential time-scale ( $\tau_{\text{decay}}$ ), logarithm of the exponential amplitude ( $\log(\Delta\nu_{\text{decay}})$ ), number of rotations added just prior to the first post-glitch ToA (or ‘phase wraps’), and the red noise spectral index and amplitude (see Liu et al. 2024). Due to the strong covariances between parameters and the lack of data near the glitch to reduce them, a no-recovery model was chosen instead (see Section 5.2).

only due to their timing parameters and inferred age, but also because of their (preliminary) deduced glitch rate and their large spin-up size and spin-down rate change. For regularly glitching neutron stars the waiting times between large glitches varies from approximately 1 yr up to about a decade (depending on the pulsar), but typical recurrence times are in the range of 1000 to 3000 d.<sup>12</sup> The description of the post-glitch recovery in such pulsars often requires one or more exponentially relaxing terms, which were not included in the models presented in Section 5.2. Yet, for PSR J0048–7317, the presence of a strong transient component following the glitch, with a large decaying amplitude and a short relaxing time-scale (see Fig. 10 for their indicative magnitudes), further strengthens the resemblance to

the Vela pulsar, for which decaying terms on similar time-scales have been identified (Dodson, McCulloch & Lewis 2002). Another very distinct characteristic of post-glitch recoveries of regular glitchers is a high value of  $\dot{\nu}$  that – once any exponential terms decay – dominates the time interval between glitches and leads to ‘anomalous’ braking indices. As can be seen from Table 2, the apparent braking index  $n = \nu\dot{\nu}/\dot{\nu}^2$  for PSR J0048–7317 is about 152, while for PSR J0040–7337  $n \simeq 91$ . This is also suggestive of possible Vela-like glitching behaviour, though it cannot be excluded that such values of  $n$  are sometimes an intrinsic property of pulsar spin-down (Parthasarathy et al. 2020). It might take a long time to confirm if that is the case as, by extrapolating from the known regularly glitching pulsars (see for example the scaling between average waiting time and  $\dot{\nu}$  presented in Haskell, Pizzochero & Sidery 2012), we estimate an average time interval between large glitches of about 3.5 yr for PSR J0040–7337 and around 6 yr for PSR J0048–7317. It remains to be seen whether these pulsars are truly Vela-like; they are

<sup>12</sup>The LMC PSR J0537–6910 also has regular large glitches, very frequently at a rate of about 3 per year (calculated with glitches of any size taken into account). It is though younger ( $\tau_c \sim 5$  kyr) and has an exceptionally high  $\dot{\nu} = -1.99 \times 10^{-10}$ .

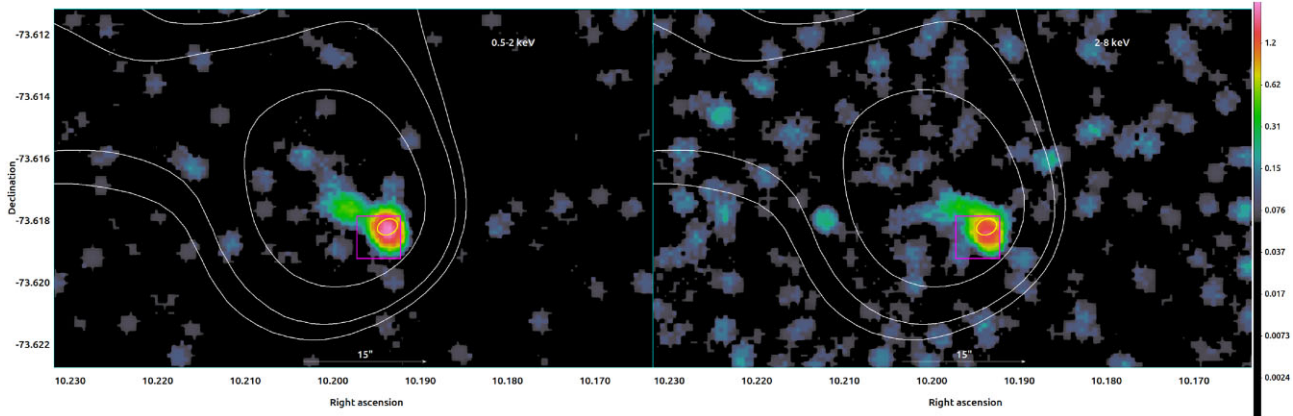


**Figure 11.** The PWN associated with PSR J0040–7337 in SNR DEM S5. The colour image is a *Chandra* counts image smoothed with a  $5''$  kernel, in the soft (left panel) and hard (right) X-rays band. A compact nebula is visible. The white contours are from the Cotton et al. (2024) radio continuum image of the SMC: only the head of the nebula is visible here, with the radio continuum tail out of the image, aligned with the X-ray tail. The innermost contour is the radio point source resolved by Alsaberi et al. (2019) in a 5500 MHz high-resolution ATCA image. The ATCA elliptical beam size with semi-axes of 1.2 arcsec in right ascension, 0.89 arcsec in declination and a position angle of  $21.3^\circ$  is displayed. Our new radio timing position for PSR J0040–7337 is shown as a magenta box, and places the pulsar at the leading edge of the bow-shock nebula.

certainly sources of interest and should be closely monitored in the future.

## 6 ASSOCIATIONS

Prior to the MeerKAT survey, all the known radio pulsars in the SMC had periods significantly larger than 100 ms, characteristic ages above 1 Myr, and spin-down luminosities spanning  $10^{32}$ – $10^{33}$  erg s $^{-1}$ . This study extends the spin parameter space of the known SMC radio pulsars to the young pulsars associated with SNRs or PWNe (see Fig. 1), like the X-ray rotation-powered SMC pulsar J0058–7218 (Maitra et al. 2021; Carli et al. 2022). We note that PSR J0048–7317 and PSR J0040–7337 are older and less energetic than the previously known young extragalactic pulsars with such associations, but are ordinary within the distribution of young Galactic pulsars.

### 6.1 PSR J0040-7337

In paper I, PSR J0040–7337 was associated with the PWN in the SNR DEM S5 (Haberl et al. 2000; Filipović et al. 2008; Alsaberi et al. 2019), due to a SEEKAT multibeam localization using the discovery observation and the period of the pulsar being indicative of a young system. In Fig. 11, we compare the radio timing position of PSR J0040–7337 with a new 97 ks *Chandra* ACIS-S image (OBSIDs 24633, 22704) centred on the PWN in SNR DEM S5. The point-like source with soft diffuse emission detected with *XMM-Newton* (Alsaberi et al. 2019) can be further resolved into a compact nebula and a point source in the *Chandra* image, which our radio timing position error region overlaps. A typical bow-shock morphology is detected in X-rays with harder emission at the position of the pulsar (as detected in the *XMM-Newton* image, Alsaberi et al. 2019), which is compatible with the radio morphology which extends further out given the longer lifetime of the radio-emitting electrons. Therefore, the position of the pulsar is consistent with the point source position and places it right behind the bow-shock.

Using the pulsar age, one can better constrain the PWN kinematics in the SNR environment, including the pulsar birth kick velocity. We note that the characteristic age from radio timing assumes a simple

magnetic dipole radiation model (introduced in Section 1) with a braking index,  $n$ , of 3 as well as a birth period much less than the current period, and thus may not reflect this pulsar’s true age. Alsaberi et al. (2019) proposed an age between 10 and 28 kyr for the pulsar-PWN system, and the characteristic age matches that upper value. For this higher age, Alsaberi et al. (2019) suggest a kick velocity of 700–800 km s $^{-1}$ , based on a distance range of 60–67.5 kpc estimated from the SMC depth. They also find that this velocity is plausible based on the PWN and SNR morphology in the local environment. This is within the known distribution of transverse velocities of bow-shock nebula pulsars, which spans 60–2000 km s $^{-1}$  (Kargaltsev et al. 2017).

It is important to consider if the kick velocity is in fact different, due to the characteristic age being an incorrect evaluation of the true age.  $\tau_c$  is related to the true age  $\tau$  as

$$\tau = \tau_c \left( 1 - \left( \frac{P}{P_{\text{birth}}} \right)^{n-1} \right) = \frac{P}{\dot{P}(n-1)} \left( 1 - \left( \frac{P}{P_{\text{birth}}} \right)^{n-1} \right), \quad (7)$$

where  $P_{\text{birth}}$  is the birth spin period of PSR J0040–7337.  $n$  is extremely difficult to measure (e.g. Johnston & Galloway 1999), though a range of 1.8–3 can be assumed (Melatos 1997). The young Galactic pulsars Vela and the Crab (PSRs J0835–4510 and J0534+2200) have had their braking indices measured to be  $1.4 \pm 0.2$  (Lyne et al. 1996) and  $2.509 \pm 0.001$  (Lyne, Pritchard & Smith 1988; Lyne, Pritchard & Graham Smith 1993), respectively, so we take a range of 1.4–3 for this calculation.

We plot the relationship between the true age, the birth period, and the kick velocity<sup>13</sup> in Fig. 12. It shows that unless the birth period was only about 10 ms shorter than the spin period is today, the kick velocity should not exceed 2000 km s $^{-1}$ . For a more realistic birth period of about 15 ms, we find that the kick velocity should be lower than 800 km s $^{-1}$ . It is not probable that the true age is much larger than the upper limit set by Alsaberi et al. (2019), and thus the kick

<sup>13</sup>We used a distance of 60 kpc, if instead we use a distance of 67.5 kpc for the Western part of the SMC (Scowcroft et al. 2016), the kick velocity for a true age of 28 kyr is 830 km s $^{-1}$ .

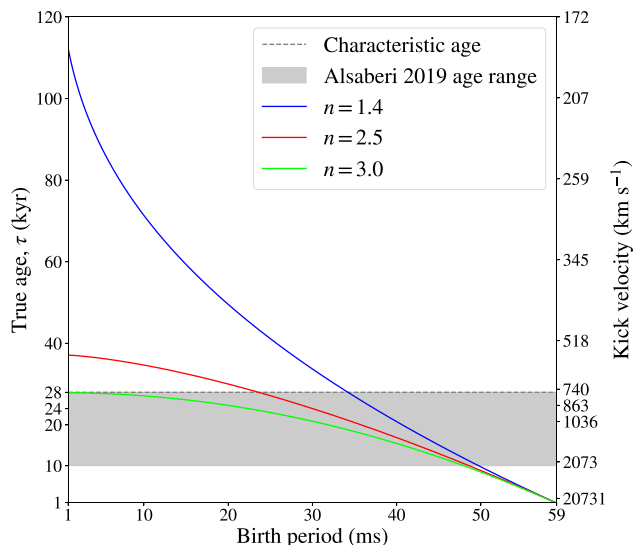


**Figure 12.** The relationship between the true age, braking index, birth period, and kick velocity of PSR J0040–7337, assuming a distance of 60 kpc.

velocity much lower, based on the PWN and SNR morphology they present. Therefore, a Vela-like true braking index is unlikely.

The proper motion of the pulsar across the sky, extrapolated from the 700–800 km s<sup>−1</sup> kick velocity range from Alsaberi et al. (2019), does not induce a significant change in the period derivative that has been measured from timing, in part due to the large distance to the system. This change, known as the Shklovskii effect (Shklovskii 1970), increases the observed period derivative by  $(6 \pm 1) \times 10^{-20}$  s s<sup>−1</sup>, which is two orders of magnitude smaller than the error on the period derivative resulting from our timing solution.

The spin-down luminosity of this pulsar is  $\dot{E}_{\text{PSR}} = 6.3 \times 10^{36}$  erg s<sup>−1</sup>. Alsaberi et al. (2019) measured the X-ray luminosity of the compact, hard X-ray emission region from the PWN and the pulsar in DEM S5 to be  $L_{\text{PWN,X}} = 1.5 \times 10^{34}$  erg s<sup>−1</sup> at a distance of 60 kpc (Karachentsev et al. 2004). The ratio of  $\frac{L_{\text{PWN,X}}}{\dot{E}_{\text{PSR}}}$  is thus about  $2.4 \times 10^{-3}$ . This so-called ‘PWN X-ray efficiency’ is similar to that of other PWNe presented in Kargaltsev et al. (2008). The PWN X-ray power-law spectral index was measured in Alsaberi et al. (2019) to be  $2 \pm 0.3$ . Kargaltsev et al. (2008) also relate the ‘PWN X-ray efficiency’ to the PWN X-ray power-law spectral index, and the values for the PWN of DEM S5 fit well within the scatter of the relationship they present.

We calculate the radio luminosity of the PWN of DEM S5, using the radio flux density and spectral index measurements from Alsaberi et al.’s (2019) table 2, with equation (4) from Frail & Scharringhausen (1997). This gives  $L_{\text{PWN,radio}} = 2.1 \times 10^{34}$  erg s<sup>−1</sup>, and a PWN radio efficiency of  $3.3 \times 10^{-3}$ . This is similar to the Vela radio pulsar-PWN system (Frail & Scharringhausen 1997). Rescaling the MeerKAT L-band discovery flux density of PSR J0040–7337 to 1400 MHz assuming a power-law radio spectral index of  $-1.60$  (Jankowski et al. 2018), we find an approximate radio flux density of  $S_{\text{PSR,1400 MHz}} \simeq 14$  μJy. We can estimate the pulsar’s radio luminosity using Szary et al.’s (2014) equation (2):  $L_{\text{PSR,1400 MHz}} \simeq 4 \times 10^{29}$  erg s<sup>−1</sup> at 60 kpc. Thus the radio efficiency of the pulsar is  $\eta_{\text{radio,PSR}} = \frac{L_{\text{PSR,1400 MHz}}}{\dot{E}_{\text{PSR}}} \simeq 6 \times 10^{-8}$ . This fits within the large scatter of the  $\eta_{\text{radio}}-\dot{E}$  relationship from Szary et al. (2014), among young pulsars with pulsed high-energy radiation and SNR association.

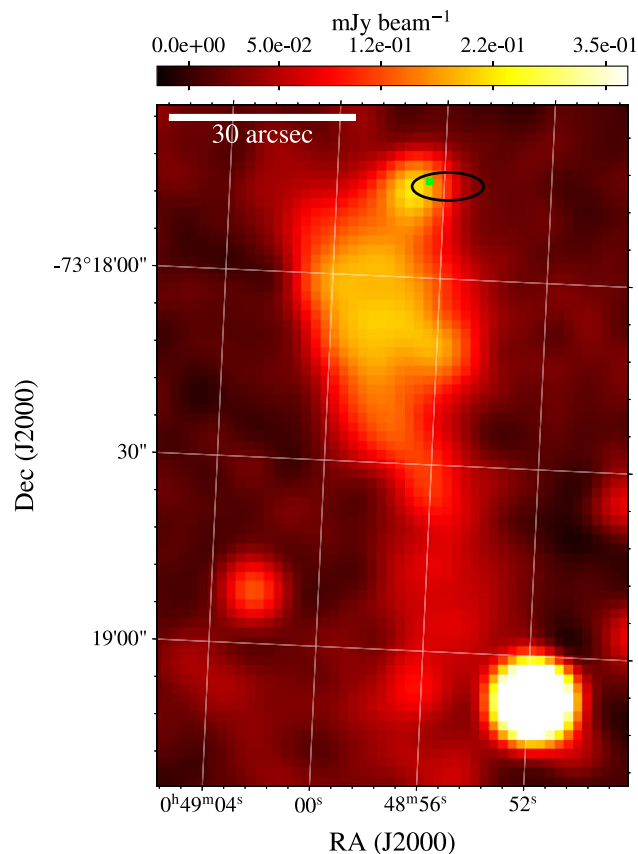


**Figure 13.** The PWN associated with PSR J0048–7317 from the Cotton et al. (2024) MeerKAT image of the SMC. The Paper I SEEKAT localization region is shown, with its  $3\sigma$  error approximated to a black ellipse. The new radio timing position is shown as a green square, and firmly places the pulsar at the leading edge of the bow-shock nebula.

According to the expected X-ray efficiency of pulsars, where the ratio of pulsed X-ray luminosity to spin-down luminosity should be around  $10^{-3}$  (Becker & Trümper 1997), we can expect PSR J0040–7337 to have a pulsed X-ray luminosity of about  $10^{33}$  erg s<sup>−1</sup> if its X-ray beam crosses our line of sight. This would be the case if the pulsar makes up for a few tenths of the total X-ray luminosity  $L_{\text{PWN}}$  (which is of the order of  $10^{34}$  erg s<sup>−1</sup>). Therefore, our radio timing localization, the low characteristic age, and large spin-down luminosity of the pulsar all confirm that PSR J0040–7337 is the engine powering the DEM S5 PWN.

## 6.2 PSR J0048-7317

In Paper I, PSR J0048–7317 was associated with a new PWN with no known parent SNR (Cotton et al. 2024). As for PSR J0040–7337, this was enabled by a SEEKAT multibeam localization using the discovery observation. Furthermore, a preliminary estimate of the period derivative of the pulsar was obtained from two survey observations, which now matches the radio timing characteristic age of 38 kyr we derive here. We show the radio timing position<sup>14</sup> of PSR J0048–7317 on the Cotton et al. (2024) radio continuum image of the new PWN in Fig. 13. Just like PSR J0040–7337, the pulsar

<sup>14</sup>This supersedes the preliminary timing position with larger errors published in Cotton et al. (2024).

is situated at the head of the radio PWN near the possible bow-shock front, with a complex and structured tail extending south of the pulsar, presumably indicating the direction of motion. The pulsar has also a characteristic age and spin-down luminosity of the same order as PSR J0040–7337, consolidating this association.

Using the same calculations as for PSR J0040–7337, we find an approximate radio flux density of  $S_{\text{PSR},1400\text{ MHz}} \simeq 49\ \mu\text{Jy}$ , and a luminosity  $L_{\text{PSR},1400\text{ MHz}} \simeq 1.3 \times 10^{30}\ \text{erg s}^{-1}$  at 60 kpc. The radio efficiency of the pulsar is  $\eta_{\text{radio,PSR}} = \frac{L_{\text{PSR},1400\text{ MHz}}}{\dot{E}_{\text{PSR}}} \simeq 5 \times 10^{-7}$ . Again, this fits within the large scatter of the  $\eta_{\text{radio}}-\dot{E}$  relationship from Szary et al. (2014), among young pulsars with pulsed high-energy radiation and SNR association, although the pulsar is in the high end of the radio luminosity distribution.

Using the radio timing position, we can constrain the X-ray flux of the pulsar-PWN system in an *XMM-Newton* 23 ks EPIC-pn observation (OBSID 0110000101). Assuming a power-law index of 1.7 and a Galactic foreground absorption of  $N_{\text{H}} = 3 \times 10^{20}\ \text{cm}^{-2}$  the unabsorbed X-ray flux upper limit in the 0.2–12 keV band is  $2.2 \times 10^{-15}\ \text{erg cm}^{-2}\ \text{s}^{-1}$ . We also take into account the sensitivity loss due to the position being off-axis in the observation. At a distance of 60 kpc, this yields an upper limit on the PWN X-ray luminosity of  $L_{\text{PWN}} \lesssim 9.5 \times 10^{32}\ \text{erg s}^{-1}$ . The ratio of  $\frac{L_{\text{PWN}}}{\dot{E}_{\text{PSR}}}$  is thus lower than  $4 \times 10^{-4}$ . This ‘PWN X-ray efficiency’ upper limit is on the low end of the distribution presented in Kargaltsev et al. (2008), but is still greater than e.g. the Vela PWN. If PSR J0048–7317 was to contribute 10 per cent of the PWN X-ray luminosity, we could expect its X-ray luminosity to be under  $10^{32}\ \text{erg s}^{-1}$ , which is below the *XMM-Newton* limiting point source luminosity in the SMC (Haberl et al. 2012). Known X-ray rotation-powered pulsars with a spin-down luminosity of  $\mathcal{O}(10^{36}\ \text{erg s}^{-1})$  have X-ray luminosities that range between  $10^{30}$  and  $10^{33}\ \text{erg s}^{-1}$  (Kargaltsev et al. 2008; Shibata et al. 2016). Therefore, this non-detection of X-rays does not rule out emission from the system. We note that our upper limit is based on a choice of absorption value and may be increased for a higher absorption level (considering PSR J0048–7317 has the highest DM in the SMC).

### 6.3 Non-associations

As stated in Paper I, the localization of PSR J0040–7335 is coincident with the SNR DEM S5, just north of the PWN of PSR J0040–7337. However, the DM of PSR J0040–7335 is nearly double that of PSR J0040–7337, so we had deemed it to be a chance background alignment. There is no multiwavelength emission detected in the images from Alsaberi et al. (2019) at the new, more precise position provided by our radio timing solution for this young, glitching pulsar; and its characteristic age does not match that of the SNR.

In Paper I, we also established that PSR J0105–7208 is unlikely to be associated with DEM S128 because of the very high implied transverse velocity given the remnant age of 12 kyr (Leahy & Filipović 2022). Here, we determine the characteristic age for the pulsar to be 206 kyr which, even given limitations on characteristic age interpretation, does not match the age of DEM S128.

## 7 CONCLUSION

We have reported nine new SMC pulsar radio timing solutions from observing campaign conducted with the MeerKAT and Murriyang telescopes with a time span of up to 3 yr, increasing the number of characterized rotation-powered extragalactic pulsars by

40 per cent. Though all pulsars we examined seem isolated, a longer timing baseline could reveal long-term binary motion (e.g. Kaspi et al. 1994). All fitted timing positions in this paper are within the  $3\sigma_{\text{SEEKAT}}$  discovery multibeam localization error presented in Paper I (except for PSR J0044–7314 for which it is within  $4\sigma$ ). Interestingly, two of the pulsars have an ‘adolescent’ characteristic age of 200 kyr, while three of the pulsars have a young characteristic age under 100 kyr and have glitched within about a year of their discovery.

The inferred glitch sizes for PSRs J0048–7317 and J0040–7337 are large, with  $\Delta\nu \gtrsim 10^{-5}\ \text{Hz}$ , but we do not have data sampled densely enough to strongly constrain a potential post-glitch exponential recovery time-scale and amplitude. For PSR J0048–7317, a transient recovery is observed, for which we can set an upper limit on the relaxation time-scale of 22 d. The positions of PSRs J0048–7317 and J0040–7337, low characteristic ages (under 40 kyr), and high spin-down luminosities (of order  $10^{36}\ \text{erg s}^{-1}$ ) confirm they are powering the PWNs they were first associated with in Paper I. Overall, these two pulsars’ characteristics as well as our first, crude, estimate of their glitching rate and their high inferred braking indices are reminiscent of the Vela pulsar. Further observations are required to confirm this, and also to consolidate a high circular polarization fraction of about 20 per cent in PSR J0048–7317: a MeerKAT observation could determine whether this fraction is greater than the linear one.

This work more than doubles the characterized population of SMC radio pulsars. This will enable an analysis of the impact of the low-metallicity, recent star formation environment of the SMC on its neutron star population and comparisons with predictions (e.g. Titus et al. 2020). We will present this population study in Paper III of this series.

## ACKNOWLEDGEMENTS

The MeerKAT telescope is operated by the South African Radio Astronomy Observatory, (SARAO) which is a facility of the National Research Foundation, an agency of the Department of Science and Innovation. SARAO acknowledges the ongoing advice and calibration of GPS systems by the National Metrology Institute of South Africa (NMISA) and the time space reference systems department of the Paris Observatory.

TRAPUM observations used the FBFUSE and APSUSE computing clusters for data acquisition, storage, and analysis. These clusters were funded and installed by the Max-Planck-Institut für Radioastronomie and the Max-Planck Gesellschaft.

Murriyang, the Parkes radio telescope, is part of the [Australia Telescope National Facility](#) which is funded by the Australian Government for operation as a National Facility managed by CSIRO (the Commonwealth Scientific and Industrial Research Organisation). We acknowledge the Wiradjuri people as the Traditional Owners of the Observatory site.

EC acknowledges funding from the United Kingdom’s Research and Innovation (UKRI) Science and Technology Facilities Council (STFC) Doctoral Training Partnership, project reference 2487536. For the purpose of open access, the author has applied a Creative Commons Attribution (CC BY) licence to any Author Accepted Manuscript version arising.

EB, MK, PVP, and VVK acknowledge continuing support from the Max Planck Society.

RPB acknowledges support from the ERC under the European Union’s Horizon 2020 research and innovation programme (grant agreement No. 715051; Spiders).

MB and AP acknowledge the resources provided by the INAF Large Grant 2022 ‘GCjewels’ (P.I. Andrea Possenti) approved with the Presidential Decree 30/2022.

DA acknowledges support from an EPSRC/STFC fellowship (EP/T017325/1).

JDT acknowledges funding from the UKRI’s STFC Doctoral Training Partnership, project reference 2659479.

This research has used the SIMBAD data base, operated at CDS, Strasbourg, France (Wenger et al. 2000), NASA’s *Astrophysics Data System* Bibliographic Services and the ATNF pulsar catalogue.

EC thanks Patrick Weltevrede, Ben Shaw, Avishek Basu, Laila Vleeschower Calas, and Iuliana Nitu for their help with pulsar software.

## DATA AVAILABILITY

The MeerKAT data underlying this article will be shared upon reasonable request to the TRAPUM collaboration. The observations parameters can be found on the *SARAO Web Archive* under observer Emma Carli or the target names specified in this publication. The Murriyang data can be downloaded from the Parkes (Murriyang) Pulsar Data Archive, accessed through CSIRO’s Data Access Portal <https://data.csiro.au/domain/atnf>, as soon as the proprietary period ends. The project codes are specified in the article.

## REFERENCES

- Alsaberi R. Z. E. et al., 2019, *MNRAS*, 486, 2507
- Anderson P. W., Itoh N., 1975, *Nature*, 256, 25
- Antonopoulou D., Espinoza C. M., Kuiper L., Andersson N., 2018, *MNRAS*, 473, 1644
- Antonopoulou D., Haskell B., Espinoza C. M., 2022, *Rep. Prog. Phys.*, 85, 126901
- Barr E. D., 2017, in Weltevrede P., Perera B. P. B., Levin L., Sanidas S. eds, Proc. IAU Symp. S337, Pulsar Astrophysics the Next Fifty Years. Cambridge Univ. Press, Cambridge, p. 175
- Basu A. et al., 2022, *MNRAS*, 510, 4049
- Becker W., Trümper J., 1997, *A&A*, 326, 682
- Bezuidenhout M. C. et al., 2023, *RAS Tech. Instrum.*, 2, 114
- Brantseg T., McEntaffer R. L., Bozzetto L. M., Filipovic M., Grieves N., 2013, *ApJ*, 780, 50
- Carli E. et al., 2022, *MNRAS*, 517, 5406
- Carli E., Levin L., Stappers B. W., Barr E. D., 2024, *MNRAS*, 531, 2835
- Carlin J. B., Melatos A., 2019, *MNRAS*, 483, 4742
- Chen W., Barr E., Karuppusamy R., Kramer M., Stappers B., 2021, *J. Astron. Instrum.*, 10, 2150013
- Clark C. J. et al., 2023, *MNRAS*, 519, 5590
- Cordes J. M., Lazio T. J. W., 2004, in Clemens D., Shah R. Y., Brainerd T. eds, ASP Conf. Ser. Vol. 317, Milky Way Surveys: The Structure and Evolution of Our Galaxy. Astron. Soc. Pac., San Francisco, p. 21
- Cotton W. D. et al., 2024, *MNRAS*, 529, 2443
- Crawford F., Kaspi V. M., Manchester R. N., Lyne A. G., Camilo F., D’Amico N., 2001, *ApJ*, 553, 367
- Dodson R. G., McCulloch P. M., Lewis D. R., 2002, *ApJ*, 564, L85
- Edwards R. T., Hobbs G. B., Manchester R. N., 2006, *MNRAS*, 372, 1549
- Ellis J. A., Vallisneri M., Taylor S. R., Baker P. T., 2020, ENTERPRISE: Enhanced Numerical Toolbox Enabling a Robust Pulsar Inference Suite, <https://doi.org/10.5281/zenodo.4059815>
- Espinoza C. M., Lyne A. G., Stappers B. W., Kramer M., 2011, *MNRAS*, 414, 1679
- Ferdman R. D., Archibald R. F., Gourgouliatos K. N., Kaspi V. M., 2018, *ApJ*, 852, 123
- Filipović M. D. et al., 2008, *A&A*, 485, 63
- Frail D. A., Scharringhausen B. R., 1997, *ApJ*, 480, 364
- Fuentes J. R., Espinoza C. M., Reisenegger A., Shaw B., Stappers B. W., Lyne A. G., 2017, *A&A*, 608, A131
- Gold T., 1968, *Nature*, 218, 731
- Gotthelf E. V., Wang Q. D., 2000, *ApJ*, 532, L117
- Haberl F., Filipović M. D., Pietsch W., Kahabka P., 2000, *A&AS*, 142, 41
- Haberl F. et al., 2012, *A&A*, 545, A128
- Harris J., Zaritsky D., 2004, *AJ*, 127, 1531
- Haskell B., Pizzochero P. M., Sidery T., 2012, *MNRAS*, 420, 658
- Ho W. C. G., Espinoza C. M., Antonopoulou D., Andersson N., 2015, *Sci. Adv.*, 1, e1500578
- Hobbs G. B., Edwards R. T., Manchester R. N., 2006, *MNRAS*, 369, 655
- Hobbs G. et al., 2020, *Publ. Astron. Soc. Aust.*, 37, e012
- Hotan A. W., van Straten W., Manchester R. N., 2004, *Publ. Astron. Soc. Aust.*, 21, 302
- Inoue H., Koyama K., Tanaka Y., 1983, in Danziger J., Gorenstein P., eds, Proc. IAU Symp. 101, Supernova Remnants and Their X-Ray Emission. Cambridge Univ. Press, Cambridge, p. 535
- Jankowski F., van Straten W., Keane E. F., Bailes M., Barr E. D., Johnston S., Kerr M., 2018, *MNRAS*, 473, 4436
- Johnston S., Galloway D., 1999, *MNRAS*, 306, L50
- Johnston S. et al., 2021, *MNRAS*, 509, 5209
- Karachentseva I. D., Karachentseva V. E., Huchtmeier W. K., Makarov D. I., 2004, *AJ*, 127, 2031
- Kargaltsev O., Pavlov G. G., Bassa C., Wang Z., Cumming A., Kaspi V. M., 2008, in Kargaltsev O., Pavlov G. G., eds, AIP Conf. Proc. Vol. 983, Pulsar Wind Nebulae in the Chandra Era. Am. Inst. Phys., New York, p. 171
- Kargaltsev O., Pavlov G. G., Klingler N., Rangelov B., 2017, *J. Plasma Phys.*, 83, 635830501
- Kaspi V. M., Johnston S., Bell J. F., Manchester R. N., Bailes M., Bessell M., Lyne A. G., D’Amico N., 1994, *ApJ*, 423, L43
- Keith M. J., Nijū I., Liu Y., 2022, run\_enterprise, <https://doi.org/10.5281/zenodo.5914351>
- Lamb R. C., Fox D. W., Macomb D. J., Prince T. A., 2002, *ApJ*, 574, L29
- Leahy D. A., Filipović M. D., 2022, *ApJ*, 931, 20
- Lehmensiek R., Theron I. P., 2012, in Graglia Roberto D., ed, 2012 International Conference on Electromagnetics in Advanced Applications. IEEE, p. 321,
- Lehmensiek R., Theron I. P., 2014, in The 8th European Conference on Antennas and Propagation (EuCAP 2014). IEEE, p. 880,
- Liu Y. et al., 2024, *MNRAS*, 532, 859
- Lorimer D., 2008, Astrophysics Source Code Library, record ascl:1107.016
- Lorimer D. R., Kramer M., 2005, Handbook of Pulsar Astronomy. Cambridge Univ. Press, Cambridge
- Lyne A. G., Pritchard R. S., Smith F. G., 1988, *MNRAS*, 233, 667
- Lyne A. G., Pritchard R. S., Graham Smith F., 1993, *MNRAS*, 265, 1003
- Lyne A. G., Pritchard R. S., Graham-Smith F., Camilo F., 1996, *Nature*, 381, 497
- Lyne A. G., Shemar S. L., Graham Smith F., 2000, *MNRAS*, 315, 534
- Maggi P. et al., 2019, *A&A*, 631, A127
- Maitra C., Ballet J., Filipović M. D., Haberl F., Tiengo A., Grieve K., Roper Q., 2015, *A&A*, 584, A41
- Maitra C., Esposito P., Tiengo A., Ballet J., Haberl F., Dai S., Filipović M. D., Pilia M., 2021, *MNRAS*, 507, L1
- Manchester R. N., Mar D. P., Lyne A. G., Kaspi V. M., Johnston S., 1993a, *ApJ*, 403, L29
- Manchester R. N., Staveley-Smith L., Kesteven M. J., 1993b, *ApJ*, 411, 756
- Manchester R. N., Hobbs G. B., Teoh A., Hobbs M., 2005, *AJ*, 129, 1993
- Manchester R. N., Fan G., Lyne A. G., Kaspi V. M., Crawford F., 2006, *ApJ*, 649, 235
- Marshall F. E., Guillemot L., Kust Harding A., Martin P., Smith D. A., 2016, in American Astronomical Society, AAS Meeting #227, id.423.04. <https://ui.adsabs.harvard.edu/abs/2016AAS...22742304M/abstract>
- Mathewson D. S., Ford V. L., Dopita M. A., Tuohy I. R., Mills B. Y., Turtle A. J., 1984, *ApJS*, 55, 189
- McCConnell D., McCulloch P. M., Hamilton P. A., Ables J. G., Hall P. J., Jacka C. E., Hunt A. J., 1991, *MNRAS*, 249, 654
- Melatos A., 1997, *MNRAS*, 288, 1049
- Men Y., Barr E., Clark C. J., Carli E., Desvignes G., 2023, *A&A*, 679, A20

- Michilli D. et al., 2018, *Nature*, 553, 182
- Middleditch J., Pennyacker C., 1985, *Nature*, 313, 659
- Middleditch J., Marshall F. E., Wang Q. D., Gotthelf E. V., Zhang W., 2006, *ApJ*, 652, 1531
- Millhouse M., Melatos A., Howitt G., Carlin J. B., Dunn L., Ashton G., 2022, *MNRAS*, 511, 3304
- Morello V., 2023, Astrophysics Source Code Library, record ascl:2310.008
- Oswald L. S. et al., 2023, *MNRAS*, 520, 4961
- Owen R. A. et al., 2011, *A&A*, 530, A132
- Padmanabh P. V., 2021, PhD thesis, Rheinische Friedrich-Wilhelms-Universität Bonn, <https://bonndoc.ulb.uni-bonn.de/xmlui/handle/20.500.11811/9336>
- Padmanabh P. V. et al., 2023, *MNRAS*, 524, 1291
- Parthasarathy A. et al., 2019, *MNRAS*, 489, 3810
- Parthasarathy A. et al., 2020, *MNRAS*, 494, 2012
- Payne J. L., White G. L., Filipović M. D., Pannuti T. G., 2007, *MNRAS*, 376, 1793
- Piro A. L., Gaensler B. M., 2018, *ApJ*, 861, 150
- Ridolfi A. et al., 2022, *A&A*, 664, A27
- Scowcroft V., Freedman W. L., Madore B. F., Monson A., Persson S. E., Rich J., Seibert M., Rigby J. R., 2016, *ApJ*, 816, 49
- Serylak M. et al., 2021, *MNRAS*, 505, 4483
- Seward F. D., Harnden F. R. J., Helfand D. J., 1984, *ApJ*, 287, L19
- Shaw B. et al., 2018, *MNRAS*, 478, 3832
- Shibata S., Watanabe E., Yatsu Y., Enoto T., Bamba A., 2016, *ApJ*, 833, 59
- Shklovskii I. S., 1970, *SvA*, 13, 562
- Standish E., 1998, Technical Report, JPL Planetary and Lunar Ephemerides
- Stappers B., Kramer M., 2016, in Taylor R., Camilo F., Leeuw L., Moodley K., eds, Proceedings of MeerKAT Science: On the Pathway to the SKA – PoS(MeerKAT2016). Sissa Medialab, Trieste, Italy, p.009
- Szary A., Zhang B., Melikidze G. I., Gil J., Xu R. X., 2014, *ApJ*, 784, 59
- Titus N., Stappers B. W., Morello V., Caleb M., Filipović M. D., McBride V. A., Ho W. C. G., Buckley D. A. H., 2019, *MNRAS*, 487, 4332
- Titus N., Toonen S., McBride V. A., Stappers B. W., Buckley D. A. H., Levin L., 2020, *MNRAS*, 494, 500
- Tuo Y., Serim M. M., Antonelli M., Ducci L., Vahdat A., Ge M., Santangelo A., Xie F., 2024, *ApJ*, 967, L13
- Van Straten W., Bailes M., 2011, *Publ. Astron. Soc. Aust.*, 28, 1
- Wang Q. D., Gotthelf E. V., 1998, *ApJ*, 494, 623
- Wang Q. D., Gotthelf E. V., Chu Y., Dickel J. R., 2001, *ApJ*, 559, 275
- Weltevrede P., 2016, *A&A*, 590, A109
- Wenger M. et al., 2000, *A&AS*, 143, 9
- Yao J. M., Manchester R. N., Wang N., 2017, *ApJ*, 835, 29

This paper has been typeset from a  $\text{\TeX}/\text{\LaTeX}$  file prepared by the author.